


























# A Community Data Set for Comparing Automated Coronal Hole Detection Schemes

Martin A. Reiss<sup>1</sup> , Karin Muglach<sup>2,3</sup> , Emily Mason<sup>4</sup> , Emma E. Davies<sup>5</sup> , Shibaji Chakraborty<sup>6</sup> , Veronique Delouille<sup>7</sup>,  
Cooper Downs<sup>4</sup> , Tadhg M. Garton<sup>8</sup> , Jeremy A. Grajeda<sup>9</sup> , Amr Hamada<sup>10,11</sup>, Stephan G. Heinemann<sup>12</sup> ,  
Stefan Hofmeister<sup>13</sup> , Egor Illarionov<sup>14,15</sup> , Robert Jarolim<sup>16</sup> , Larisza Krista<sup>17,18</sup> , Chris Lowder<sup>19</sup>, Erwin Verwichte<sup>20</sup> ,  
Charles N. Arge<sup>2</sup> , Laura E. Boucheron<sup>9</sup> , Claire Foullon<sup>21</sup> , Michael S. Kirk<sup>2</sup> , Alexander Kosovichev<sup>22,23,24</sup> ,  
Andrew Leisner<sup>25</sup> , Christian Möstl<sup>5</sup> , James Turtle<sup>4</sup> , and Astrid Veronig<sup>16</sup> 

<sup>1</sup> Community Coordinated Modeling Center, NASA Goddard Space Flight Center, 8800 Greenbelt Rd., Greenbelt, MD 20771, USA; [martin.a.reiss@outlook.com](mailto:martin.a.reiss@outlook.com)

<sup>2</sup> NASA Goddard Space Flight Center, 8800 Greenbelt Rd., Greenbelt, MD 20771, USA

<sup>3</sup> Catholic University of America, Washington, DC 20064, USA

<sup>4</sup> Predictive Science Inc., 9990 Mesa Rim Rd., Suite 170, San Diego, CA 92121, USA

<sup>5</sup> Austrian Space Weather Office, GeoSphere Austria, Graz, A-8020, Austria

<sup>6</sup> Center for Space Science and Engineering Research, Virginia Tech, Blacksburg, VA, USA

<sup>7</sup> Royal Observatory of Belgium, Brussels, Belgium

<sup>8</sup> Manakau Ltd., Dublin, Ireland

<sup>9</sup> Klipsch School of Electrical and Computer Engineering, New Mexico State University, Las Cruces, NM 88003, USA

<sup>10</sup> National Solar Observatory, Boulder, CO 80303, USA

<sup>11</sup> University of Colorado Boulder, Boulder, CO 80309, USA

<sup>12</sup> Department of Physics, University of Helsinki, P.O. Box 64, FI-00014, Helsinki, Finland

<sup>13</sup> Leibniz Institute for Astrophysics, Potsdam, Germany

<sup>14</sup> Moscow State University, Moscow, 119991, Russia

<sup>15</sup> Moscow Center of Fundamental and Applied Mathematics, Moscow, 119234, Russia

<sup>16</sup> University of Graz, Graz, Austria

<sup>17</sup> Cooperative Institute for Research in Environmental Sciences, University of Colorado, Boulder, CO 80309, USA

<sup>18</sup> National Centers for Environmental Information, National Oceanic and Atmospheric Administration, Boulder, CO 80305, USA

<sup>19</sup> Southwest Research Institute, Boulder, CO 80302, USA

<sup>20</sup> Department of Physics, University of Warwick, Coventry, CV4 7AL, UK

<sup>21</sup> Department of Mathematics and Statistics, University of Exeter, Exeter, EX4 4QF, UK

<sup>22</sup> Center for Computational Heliophysics, New Jersey Institute of Technology, Newark, NJ 07102, USA

<sup>23</sup> Department of Physics, New Jersey Institute of Technology, Newark, NJ 07102, USA

<sup>24</sup> NASA Ames Research Center, Moffett Field, CA 94035, USA

<sup>25</sup> Department of Physics and Astronomy, George Mason University, Fairfax, VA 22030, USA

Received 2023 August 21; revised 2023 December 6; accepted 2023 December 6; published 2024 February 13

## Abstract

Automated detection schemes are nowadays the standard approach for locating coronal holes in extreme-UV images from the Solar Dynamics Observatory (SDO). However, factors such as the noisy nature of solar imagery, instrumental effects, and others make it challenging to identify coronal holes using these automated schemes. While discrepancies between detection schemes have been noted in the literature, a comprehensive assessment of these discrepancies is still lacking. The contribution of the Coronal Hole Boundary Working Team in the COSPAR ISWAT initiative to close this gap is threefold. First, we present the first community data set for comparing automated coronal hole detection schemes. This data set consists of 29 SDO images, all of which were selected by experienced observers to challenge automated schemes. Second, we use this community data set as input to 14 widely applied automated schemes to study coronal holes and collect their detection results. Third, we study three SDO images from the data set that exemplify the most important lessons learned from this effort. Our findings show that the choice of the automated detection scheme can have a significant effect on the physical properties of coronal holes, and we discuss the implications of these findings for open questions in solar and heliospheric physics. We envision that this community data set will serve the scientific community as a benchmark data set for future developments in the field.

*Unified Astronomy Thesaurus concepts:* [Solar coronal holes \(1484\)](#); [Solar corona \(1483\)](#); [Solar wind \(1534\)](#)

## 1. Introduction

The open magnetic field components of the solar magnetic field are often observed in extreme-UV (EUV) and soft X-ray (SXR) images as darker, cooler, and less dense patches in the corona, known as “coronal holes.” Knowing how coronal holes manifest themselves in the solar corona goes hand in hand with understanding the origin of the heliosphere. Spacecraft missions

such as the Solar Dynamics Observatory (SDO; Pesnell et al. 2012) observe the corona with unprecedented quality and quantity. Since the beginning of the operational phase in 2010 May, approximately 1.5 TB of data have been downlinked from the SDO spacecraft to Earth daily, resulting in about 5 PB of archived data up to now. For this reason, as well as others discussed below, a shift from manual to automated coronal hole detection occurred during the SDO era, leading to a preference for automated coronal hole detection schemes rather than coronal hole boundaries being outlined by experienced observers (see Section 2). These automated schemes have facilitated progress, but questions about interpreting their results remain.



Original content from this work may be used under the terms of the [Creative Commons Attribution 4.0 licence](#). Any further distribution of this work must maintain attribution to the author(s) and the title of the work, journal citation and DOI.

Some questions are as follows: Why do different coronal hole detection schemes give different results? How does the choice of the detection scheme affect the coronal hole locations in EUV and SXR images, and how significant are these differences? Quantitative comparisons between different schemes have received little attention until recently; it is also unclear whether some schemes are prone to systematic errors. What are the effects of these errors on the statistical assessment of coronal holes? Lastly, and most importantly, how does the choice of automated schemes affect our understanding of coronal holes? Addressing these questions is the focus of the Coronal Hole Boundary Working Team,<sup>26</sup> a community effort embedded in the COSPAR ISWAT initiative.<sup>27</sup> Recent results give justification for these questions (Linker et al. 2021; Reiss et al. 2021), and answering them might lead to a better understanding of the global coronal magnetic field.

Traditionally, the global coronal magnetic field has been divided into regions of open and closed magnetic fields (Mackay & Yeates 2012; Priest 2014). Open-field lines stretch out into the heliosphere and become part of the interplanetary magnetic field. Scientists expect that most coronal footpoints of open-field lines are visible as dark patches—coronal holes—in observations of the EUV and SXR corona (Newkirk 1967; Munro & Withbroe 1972; Zirker 1977).

In contrast to open-field lines, closed-field lines confine the coronal plasma, leading to the formation of an equatorial streamer belt. This equatorial streamer belt is associated with “helmet streamers” that stretch across the neutral line at the Sun and extend to create the heliospheric current sheet. The streamer belt is most prominent during the solar minimum period. It is best observed in coronagraph and eclipse images of the corona when the neutral line is oriented horizontally, meaning in an east–west direction (see Wang et al. 1997).

Identifying coronal holes in EUV and SXR images offers valuable observational context for unsolved questions about the origin, formation, and evolution of the solar wind flow and its embedded magnetic field (see McComas et al. 2007; Linker et al. 2017; Viall & Borovsky 2020; among others). NASA’s SDO mission has provided us with one of the richest repositories of solar imaging data in UV and EUV, which has sparked increased interest in automated coronal hole detection. Dozens of automated schemes have been developed, and this study will compare many of them for the first time.

We first consider the underlying physical processes before addressing why various automated detection schemes give different results. The dynamic nature of the corona makes the automated detection of coronal holes, and their boundaries in particular, challenging in solar images. The evolution of the coronal hole boundary at short timescales is primarily governed by the interplay between open and closed magnetic fields in a process called “interchange reconnection” (e.g., Nash et al. 1988). Interchange reconnection occurs between open-field lines inside coronal holes and small closed loops (e.g., ephemeral regions and intra-network), and between open-field lines and large-scale closed loops along coronal hole boundaries. The latter may decouple the coronal hole boundaries from the underlying photospheric field rotation, explaining why coronal holes exhibit a rotation rate different from the underlying photospheric plasma (Timothy et al. 1975; Wang & Sheeley 1993; Krista et al. 2018; Heinemann et al. 2020). Individual photospheric flux

elements continuously cross these boundaries, transforming their associated field lines from closed to open as they enter the hole and from open to closed as they exit it. Besides large-scale processes in which reconnection occurs high in the corona at the streamer cusps, small-scale reconnection may also occur randomly at the boundaries. Such a random process may jostle the coronal hole boundaries back and forth on short timescales. The findings in Mason & Uritsky (2022) support the existence of small-scale interchange reconnection at coronal hole boundaries. This dynamic evolution of coronal hole boundaries may help explain why automated schemes show discrepancies on a small scale. Both small- and large-scale processes challenge automated schemes to define these “fuzzy” coronal hole boundaries uniquely.

Beyond interchange reconnection at the coronal hole boundaries, instrumental effects and other factors further complicate the detection of coronal holes (Toma & Arge 2005). These include (a) the varying intensities of coronal holes observed in EUV and SXR filters, as these filters are sensitive to different plasma temperatures, (b) large, bright coronal loops close to coronal holes, partially obscuring the coronal hole (Wang 2017), (c) changes in viewing angle caused by solar rotation (Wang 2017), (d) the similar EUV intensities of coronal holes to other solar structures, such as filaments (Reiss et al. 2015) or active-region canopies (Wang et al. 2011), which can lead to the misidentification of a closed-field structure as an open-field structure, (e) the effect of stray light from surrounding brighter regions (Saqri et al. 2020), and (f) the noisy nature of EUV images and other systematic instrumental effects, as mentioned in Caplan et al. (2016). Considering that all these factors are handled differently in existing automated schemes, it is not surprising that coronal hole detection results show discrepancies.

A promising avenue to identify the footpoint locations of open-field regions is to consult global coronal magnetic models. Linker et al. (2017) argue that, if the prevailing view of the global coronal magnetic field is correct, one would expect that model solutions will match observations. More specifically, the footpoint location of open-field lines that reach a given height (often 2.5 solar radii) above the photosphere should match coronal hole observations in EUV and SXR images. To some extent, coronal hole observations agree with potential magnetic field models and force-free field extrapolations on a global scale (Wallace et al. 2019). However, the agreement is not as clear on a smaller scale. Linker et al. (2017) found that existing models could not simultaneously meet two fundamental constraints. First, that the magnetic flux from coronal open-field regions matches in situ spacecraft measurements; and, second, that the open-field regions in models correspond to observed regions of lower emission in EUV and SXR images. Explanations for solving this “open flux problem” have received much attention but are not without debate (Riley 2007; Wang & Sheeley 2015; Linker et al. 2017, 2021; Riley et al. 2019; Badman et al. 2021; Frost et al. 2022; Wang et al. 2022; Arge et al. 2023). A better understanding of the uncertainties in coronal hole observations could therefore provide powerful constraints for state-of-the-art models of the large-scale corona and inner heliosphere.

Much of our current knowledge of coronal holes has been inferred from SDO observations using automated detection schemes, despite little attention having been paid to what effect

<sup>26</sup> [www.iswat-cospar.org/s2-01](http://www.iswat-cospar.org/s2-01)

<sup>27</sup> [www.iswat-cospar.org](http://www.iswat-cospar.org)

the choice of detection scheme has. The Coronal Hole Boundary Working Team was formed to answer the following open questions:

1. How significant are the observational uncertainties of coronal hole boundaries in automated detection schemes?
2. To what extent does this uncertainty affect our understanding of coronal holes?
3. How can our activities support the research community in the long term?
4. How can we use these uncertainties to improve our space-weather modeling capabilities?

In this current study, we focus on the first three questions; subsequent research will be dedicated to the last question.

By tying together the expertise in coronal hole detection worldwide, this study compares the results of 14 automated coronal hole detection schemes, which is the most comprehensive comparison to date. We present an open data set containing 29 SDO images to challenge automated schemes and thereby provide the community with a reference point for future developments. We will show that there are systematic discrepancies across schemes, and that the choice of detection scheme can significantly influence coronal hole boundary locations. These results support our findings in Reiss et al. (2021), where we studied a coronal hole at the solar disk center on 2018 May 30 and compared the boundaries identified by nine different detection schemes.

This paper is structured as follows. Section 2 discusses community schemes for locating coronal holes in SDO mission data. Section 3 introduces our SDO data catalog and explains the image data preparation, while Section 4 presents three examples that illustrate the lessons learned. The discussion in Section 5 concludes our study and outlines future perspectives.

## 2. The Solar Dynamics Observatory and Coronal Hole Detection

On the late morning of 2010 February 11, the Atlas V rocket thundered off from the Space Launch Complex 41 in Cape Canaveral, Florida, to lift the SDO (Pesnell et al. 2012) into orbit. On board were the Atmospheric Imaging Assembly (AIA; Lemen et al. 2012), the Extreme Ultraviolet Variability Experiment (EVE; Woods et al. 2012), and the Helioseismic and Magnetic Imager (HMI; Scherrer et al. 2012). Together these instruments provided observations of the Sun in unprecedented quantity and quality. Since the operational phase began on 2010 May 14, SDO has monitored the Sun in seven EUV wave bands ranging between 94 Å and 335 Å.

Historically, observers first noted regions on the Sun with strongly reduced emission in rocket-borne spectroheliographs (Tousey et al. 1968). A few years later, Skylab, the first United States space station, revealed more detail about these “coronal holes.” The Apollo Telescope Mount on board the space station observed the physical conditions in coronal holes simultaneously in the solar chromosphere, transition region, and the corona (Huber et al. 1974). Since these discoveries in the 1970s, many ground- and space-based instruments have been used to monitor coronal holes in different wavelengths. The spectrum of wavelengths for coronal hole observations includes radio, near-infrared (He I 10830 Å), coronagraphic white light, EUV, and SXR. The sizes and shapes of coronal holes vary between wavelengths due to the differing formation heights of the dominant emission in the respective wave bands.

Interpreting these collective observations led to a broader understanding of coronal holes, particularly their plasma and magnetic properties (Zirker 1977; Cranmer 2009), locations (Hofmeister et al. 2017; Lowder et al. 2017), temporal and spatial evolution (Heinemann et al. 2018; Krista et al. 2018), and their importance for the evolving solar wind flows and embedded magnetic fields (Wang & Sheeley 1990). These insights also helped develop models of the large-scale corona and inner heliosphere (see, e.g., Wang & Sheeley 1990; Mikić et al. 1999; Arge & Pizzo 2000; Riley et al. 2001; Arge et al. 2003; Tóth et al. 2005; van der Holst et al. 2014). In the past, manual outlining of coronal holes by experienced observers was the standard approach in locating coronal holes in solar observations (see, e.g., Harvey & Recely 2002; McIntosh 2003). Since manual outlining of coronal holes is time consuming and hand-drawn maps are often unavailable in digital form, automated detection schemes have received significant attention from the community.

Using ground-based observations of the Sun, Henney & Harvey (2005) developed the first automated coronal hole detection scheme. Dozens of automated schemes followed, relying on either ground-based and space-based instruments or a combination of both (see Malanushenko & Jones 2005; Toma & Arge 2005; Scholl & Habbal 2008). Over more than a decade, the AIA instrument on board the SDO spacecraft has assembled a rich repository of coronal hole observations, unmatched in both quantity and quality. Therefore, we focus this comparison to schemes that use SDO data products as the inputs. Many of these schemes will be compared here for the first time, with their discrepancies quantified.

At the heart of each detection scheme lies a thresholding strategy. Intensity-based thresholding is the most common strategy for detecting coronal holes in EUV and SXR images. The challenge is to identify an intensity threshold that best separates coronal holes from the surrounding closed-field plasma regions. For example, SPoCA-CH uses fuzzy C-means clustering, an iterative clustering algorithm that associates the class with the lowest intensity with coronal holes (Delouille et al. 2018). Class centers are computed over a 10 yr period and remain fixed. On the other hand, SPoCA-HEK (running at LMSAL since 2009) computes class centers over a rolling time window of 3 days. A further example, Active Contours Without Edges (ACWE), approaches coronal hole detection based on the homogeneity of intensities rather than absolute intensity values. A comprehensive discussion of ACWE is given in Appendix A, Boucheron et al. (2016), and Grajeda et al. (2023).

Another common thresholding strategy uses partitioning of full-disk images into subframes. Coronal Hole Automated Recognition and Monitoring (CHARM; Krista & Gallagher 2009) and Coronal Hole Observer and Regional Tracker for Long-term Examination (CHORTLE; Lowder et al. 2014) are examples. CHARM uses 193 Å observations to identify dark regions, and uses magnetograms to distinguish between coronal holes and filaments. In contrast, Synoptic Coronal Hole Maps (SYNCH) partitions images into subframes and simultaneously uses three wavelengths (171 Å, 193 Å, and 304 Å) to detect coronal holes (Hamada et al. 2018). A further scheme, Coronal Hole Identification via Multi-thermal Emission Recognition Algorithm (CHIMERA), also uses three wavelengths (171 Å, 193 Å, and 211 Å) and performs a conjunction of color segmentations to separate regions. This color segmentation method, combined with the different peak

observation temperatures in each passband, acts as a stand-in for a thermal- and density-based segmentation method. Regions that are identified as significantly cooler than the surrounding corona are then checked for sufficient size and monopolarity to separate coronal holes from possible cool quiet-Sun regions (see Garton et al. 2018). Warwick wavelet watershed-based coronal segmentation (WWWBCS) uses wavelet filtering and watershed segmentation to create uniform regions to improve the statistics of clustering in a three-parameter space built from the 171 Å, 193 Å, and 211 Å wave bands (see Appendix C and Foullon & Verwichte 2006).

Similar to the previous schemes, Coronal Hole Identification using a Probabilistic Scheme (CHIPS) also utilizes the 171 Å, 193 Å and 211 Å wave bands. However, it distinguishes itself from other schemes by employing a probabilistic approach that inherently provides measures of uncertainty for coronal hole locations.

A unique scheme, referred to as the Coronal Hole Mapping and Analysis Pipeline (CHMAP), was proposed in Caplan et al. (2016), where the coronal hole maps are calculated from simultaneous multi-instrument EUV images. These so-called “synchronic” EUV maps are promising for studying the spatial and temporal evolution of coronal holes.

More recently, data science has enabled the development of automated schemes that surrogate a human observer. CNN193 uses a neural network to locate coronal holes in the widely used 193 Å wavelength (Illarionov & Tlatov 2018). The neural network is trained on coronal hole segmentation maps which solar scientists have supervised. Similarly, Coronal Hole Recognition Neural Network Over multi-Spectral-data (CHRONNOS) trains a neural network but uses six EUV filtergrams of AIA and the HMI line-of-sight (LOS) magnetic maps as input (Jarolim et al. 2021).

Besides fully automated detection schemes, there are also schemes that include human supervision. An example is Collection of Analysis Tools for Coronal Holes (CATCH), which uses an automated coronal hole detection scheme to extract the coronal hole boundary at the location where the intensity gradient is maximal (Heinemann et al. 2019). All the detected regions by CATCH need to be inspected by a human observer and filaments removed later by hand.

To compare the established schemes with a simple detection strategy, we have defined a reference scheme called TH35. The intensity threshold is calculated as 35% of the average intensity on the solar disk, without any postprocessing of the coronal hole maps.

For a more thorough discussion of the schemes in this study, we refer the reader to Table 1, which includes references and links that explain the individual methodologies.

### 3. A Community Data Set for Comparing Automated Coronal Hole Detection Schemes

We present the first community data set developed for comparing the results of automated coronal hole detection schemes. In creating this open data set, we aim to address these four objectives:

1. Support the solar and heliospheric science community by providing an unbiased reference data set for developing improved automated coronal hole detection capabilities.

2. Identify and quantify the strengths and weaknesses of automated detection schemes that are widely used in the scientific community.
3. Increase awareness that the choice of the detection scheme may significantly affect the size and shape of coronal hole regions, and thus the interpretation of the results.
4. Pave the way for coronal hole products with inherent measures of uncertainty as observational constraints for global magnetic models of the solar corona.

To achieve these objectives, we have collected a community data set of 29 SDO images observed between the years 2014 and 2019, spanning from maximum solar activity to the following minimum.

We selected these dates to challenge automated detection schemes. Table 2 gives the image dates, lists the magnetic structures found at coronal hole boundaries, and provides information on the availability of supplementary observations from the STEREO-A spacecraft (Kaiser 2005) and the K-Coronagraph (K-Cor) operated by the Mauna Loa Solar Observatory (de Wijn et al. 2012).

For each date, the data set provides all seven EUV wave bands ranging from 94 Å to 335 Å from the AIA instrument, and the LOS measurements of the photospheric magnetic field from the HMI instrument. Additionally, we use 193 Å images to visually identify coronal holes and filaments, and label them in all 29 images for an event-based analysis. Examples of these annotated images are discussed in Section 4.4. All labeled images, along with the original AIA images and coronal hole identifications, are available to the community.

The SDO data platform archives solar images as level 1.0 data, where data calibration procedures have already been applied. We downloaded all the selected images from the SDO data archive and used the SolarSoft<sup>28</sup> routine `aia_prep.pro`. This routine removes shifts between the different AIA filters by recentering the images, corrects the roll angle to align east–west and north–south to the  $x$ -axis and  $y$ -axis, and scales all images to the same resolution of  $0.6 \text{ pixel}^{-1}$ . We also applied `hmi_prep.pro` to HMI measurements of the LOS component of the photospheric field to make the same corrections and align the magnetograms to the EUV images. We selected the LOS magnetogram (measured every 45 s) that is closest in time to the AIA images so that the magnetogram matches the AIA data to less than a pixel.

We provided the complete data set to all the research teams listed in Table 1 and collected the resulting coronal hole maps. The data set, including the coronal hole detections from the schemes in Table 1, is publicly available online at doi:[10.6084/m9.figshare.23997993.v1](https://doi.org/10.6084/m9.figshare.23997993.v1).

The information on the bordering magnetic structures in Table 2 was determined using the widest available combination of observational data at the time of observation. This included (in addition to AIA data) EUVI data from STEREO-A, white-light coronagraph data from MLSO K-Cor, and potential-field source-surface (PFSS) extrapolations created from the SolarSoft tool `pfss_viewer`. We analyzed the regions over several days to capture as much information as possible, both on the limb and on disk, to determine into which of the four major categories the neighboring closed structures fell. These categories were helmet streamer (HS), pseudostreamer (PS),

<sup>28</sup> <https://soho.nascom.nasa.gov/solarsoft/>

**Table 1**  
Overview of Automated Coronal Hole Detection Schemes Included in the Comparison

Short Name (1)	Research Institution (2)	Reference (3)	Input Wave Band (4)	Online Platform (5)
ACWE	New Mexico State University	Boucheron et al. (2016) and Appendix A	193 Å	<a href="https://github.com/DuckDuckPig/CH-ACWE">https://github.com/DuckDuckPig/CH-ACWE</a>
CATCH <sup>a</sup>	University of Graz	Heinemann et al. (2019)	193 Å	<a href="https://github.com/sgheinemann/CATCH">https://github.com/sgheinemann/CATCH</a>
CHARM	University of Colorado	Krista & Gallagher (2009)	193 Å, line-of-sight (LOS) magnetogram	<a href="https://github.com/larizakrista/CHARM">https://github.com/larizakrista/CHARM</a>
CHIMERA	Trinity College Dublin	Garton et al. (2018) Appendix B	171 Å, 193 Å, 211 Å, LOS magnetogram	<a href="https://github.com/TCDSolar/CHIMERA">https://github.com/TCDSolar/CHIMERA</a>
CHIPS	Virginia Tech	...	171 Å, 193 Å, 211 Å	...
CHMAP	Predictive Science Inc.	Caplan et al. (2016)	193 Å(SDO) and 195 Å (STEREO)	<a href="https://github.com/predsci/CHMAP">https://github.com/predsci/CHMAP</a>
CHORTLE	Southwest Research Institute	Lowder et al. (2014)	193 Å, LOS magnetogram	<a href="https://github.com/lowderchris/CHORTLE">https://github.com/lowderchris/CHORTLE</a>
CHRONNOS	University of Graz	Jarolim et al. (2021)	94 Å, 131 Å, 171 Å, 193 Å, 211 Å, 304 Å, 335 Å, LOS magnetogram	<a href="https://github.com/RobertJaro/MultiChannelCHDetection">https://github.com/RobertJaro/MultiChannelCHDetection</a>
CNN193	Moscow State University	Illarionov & Tlatov (2018)	193 Å	<a href="https://github.com/observethesun/coronal_holes">https://github.com/observethesun/coronal_holes</a>
SPoCA-CH	Royal Observatory of Belgium	Delouille et al. (2018)	193 Å	<a href="http://swhv.oma.be/user_manual/">http://swhv.oma.be/user_manual/</a>
SPoCA-HEK	Royal Observatory of Belgium	Verbeeck et al. (2014)	193 Å	...
SYNCH	University of Oulu	Hamada et al. (2018)	171 Å, 193 Å, 304 Å	<a href="http://satdat.oulu.fi/solar_data/">http://satdat.oulu.fi/solar_data/</a>
TH35 <sup>b</sup>	...	...	193 Å	...
WWWBCS	University of Warwick	Appendix C	171 Å, 193 Å, 211 Å	...

**Notes.** Abbreviations: ACWE: Active Contours Without Edges; CATCH: Collection of Analysis Tools for Coronal Holes; CHARM: Coronal Hole Automated Recognition and Monitoring; CHIMERA: Coronal Hole Identification via Multi-thermal Emission Recognition Algorithm; CHIPS: Coronal Hole Identification using a Probabilistic Scheme; CHMAP: Coronal Hole Mapping and Analysis Pipeline; CHORTLE: Coronal Hole Observer and Regional Tracker for Long-term Examination; CHRONNOS: Coronal Hole Recognition Neural Network Over multi-Spectral-data; CNN193: convolutional neural network; SPoCA: Spatial Possibilistic Clustering Algorithm; SYNCH: Synoptic Coronal Hole Maps; TH35: threshold-based segmentation; WWWBCS: Warwick wavelet watershed-based coronal segmentation.

<sup>a</sup> CATCH is the only scheme in this study that is not automated. It is a supervised detection scheme where the user makes the final selection.

<sup>b</sup> TH35 is a baseline against which other schemes can be compared.

filament (Fil), and active region (AR). Strictly topologically speaking, every boundary could be defined simply as a HS or PS, but as the analysis progressed it was apparent that filaments and active regions that were very close to the coronal hole boundary generated a visibly different boundary appearance than those that were created by quiet-Sun HSs or PSs. For all dates, the K-Cor data were used to identify HS/PS locations, while the PFSS model was used for confirmation purposes only. The EUV data were used on disk to identify the Fil and AR locations, and on the limb to correlate boundaries with the white-light data. An example of these labeled areas can be found in panels (b), (d), and (f) of Figure 1.

## 4. Results

To demonstrate the variation between automated detection schemes, we study the results of the schemes applied to three SDO images taken on 2015 August 20, 2018 June 23, and 2015 August 11 from the community data set. In addition, we provide a statistical analysis of the different schemes applied to all 29 SDO images in this new community data set.

### 4.1. Example I: 2018 June 23

We study the SDO image from our community data set recorded on 2018 June 23. Many automated schemes in this study are applied to identify coronal holes and link their physical properties to the conditions in near-Earth space. Figure 2 shows that on 2018 June 26, the SWEPAM instrument

aboard the Advanced Composition Explorer (ACE) spacecraft detected the arrival of high-speed solar wind at L1. The bulk speed reached over  $600 \text{ km s}^{-1}$  at approximately 14:00 UT. The geomagnetic storm began on 2018 June 25, in the slow solar wind ahead of the arrival of the fast solar wind. It started around the time of the heliospheric current sheet crossing in the stream-interacting region, and was not directly caused by the later arrival of the fast solar wind on 2018 June 26.

Figure 3 shows the full-disk image observed by SDO/AIA 193 Å, which is dominated by the Fe XII line emissions at a formation temperature of approximately 1.6 MK, on 2018 June 23. The overlaid coronal hole boundaries were detected by different automated schemes. The most prominent features are a northern and southern polar coronal hole, and an equatorial coronal hole that persisted for several Carrington rotations. When studying the equatorial coronal hole, we find that the shapes and sizes of the hole boundaries detected by different schemes vary significantly. ACWE, SPoCA-CH, and TH35 primarily detect smaller areas, while schemes like CNN193, CHIPS, CHORTLE, and WWWBCS show significantly larger areas for the equatorial coronal hole.

We identify the coronal hole at disk center as the most plausible origin of the high-speed stream arriving at Earth approximately 3 days later. We established this link by consulting publicly available magnetic connectivity tools online, all of which confirmed the equatorial coronal hole as the source region. Figure 4 presents a detailed analysis of this coronal hole at the disk center. Each detection scheme creates a

**Table 2**  
Overview of the SDO/AIA Images in the Community Data Set including the Different Magnetic Structures at the Coronal Hole Boundaries

Date	NPCH	SPCH	EqCH	K-Cor	STA	Sep. Angle (deg)
2014-07-15	HS	Fil/HS/NPT	Questionable; HS	no	yes	163
2014-10-02	HS/Fil/PS	Fil	...	no	yes	169
2015-01-04	PS/HS	Fil/HS	...	no	no	172
2015-01-21	HS/PS	HS/PS	...	yes	no	173
2015-02-10	HS/Fil	HS/Fil	Everything	no	no	174
2015-03-31	HS	HS/AR	...	no	no	177
2015-04-18	Fil/AR/HS	HS/PS	PS	yes	no	178
2015-06-06	N/A	Fil	Fil/AR/HS	yes	no	179
2015-08-11	AR/HS/Fil	Fil/AR	Everything	yes	yes	173
2015-08-18	HS/Fil	HS	HS	yes	no	173
2015-08-20	HS	HS	HS	yes	no	173
2015-09-23	N/A	Fil/AR/HS	...	yes	no	170
2015-11-07	HS/AR	HS	...	yes	no	168
2016-01-14	N/A	HS	...	yes	yes	165
2016-03-05	HS/AR	HS	HS	yes	yes	163
2016-03-18	PS/Fil/HS	HS	...	yes	yes	162
2016-03-26	HS	HS	...	yes	yes	162
2016-09-02	Fil/PS	N/A	...	yes	yes	150
2016-12-19	PS/AR/HS	HS	HS/AR	no	yes	144
2016-12-28	Fil/HS	HS	AR/Fil	yes	yes	144
2017-01-03	Fil	HS	...	no	yes	144
2017-09-25	PS/AR/HS	PS/HS	...	yes	yes	127
2017-10-04	PS/HS	HS	HS/AR	yes	yes	126
2018-03-13	HS	HS	HS/AR	no	yes	119
2018-05-30	HS	Fil/HS	HS/AR	yes	yes	115
2018-06-09	HS	Fil	HS	yes	yes	114
2018-06-23	HS	Fil/HS	Questionable	yes	yes	113
2019-05-04	HS	HS	...	no	yes	95
2019-06-16	Fil/HS	HS	...	yes	yes	92

**Notes.** This overview is meant for the major border regions and does not include every small extension or corridor that may or may not exist on a border. The last three columns show data availability of the K-coronagraph (K-Cor), STEREO-A spacecraft, and the STEREO-A separation angle. If there are two structures listed, it refers to those visible at or near the east and west limb on the listed date, respectively. If there are three structures listed, it refers to the structures visible closest to the east limb, disk center, and west limb on the listed date, respectively. The SDO images with dates in bold are studied in greater detail in Section 4. Abbreviations: north pole coronal hole (NPCH), south pole coronal hole (SPCH), equatorial CH (EqCH), helmet streamer (HS), pseudostreamer (PS), filament (Fil), null-point topology (NPT), active region (AR), and STEREO-A (STA).

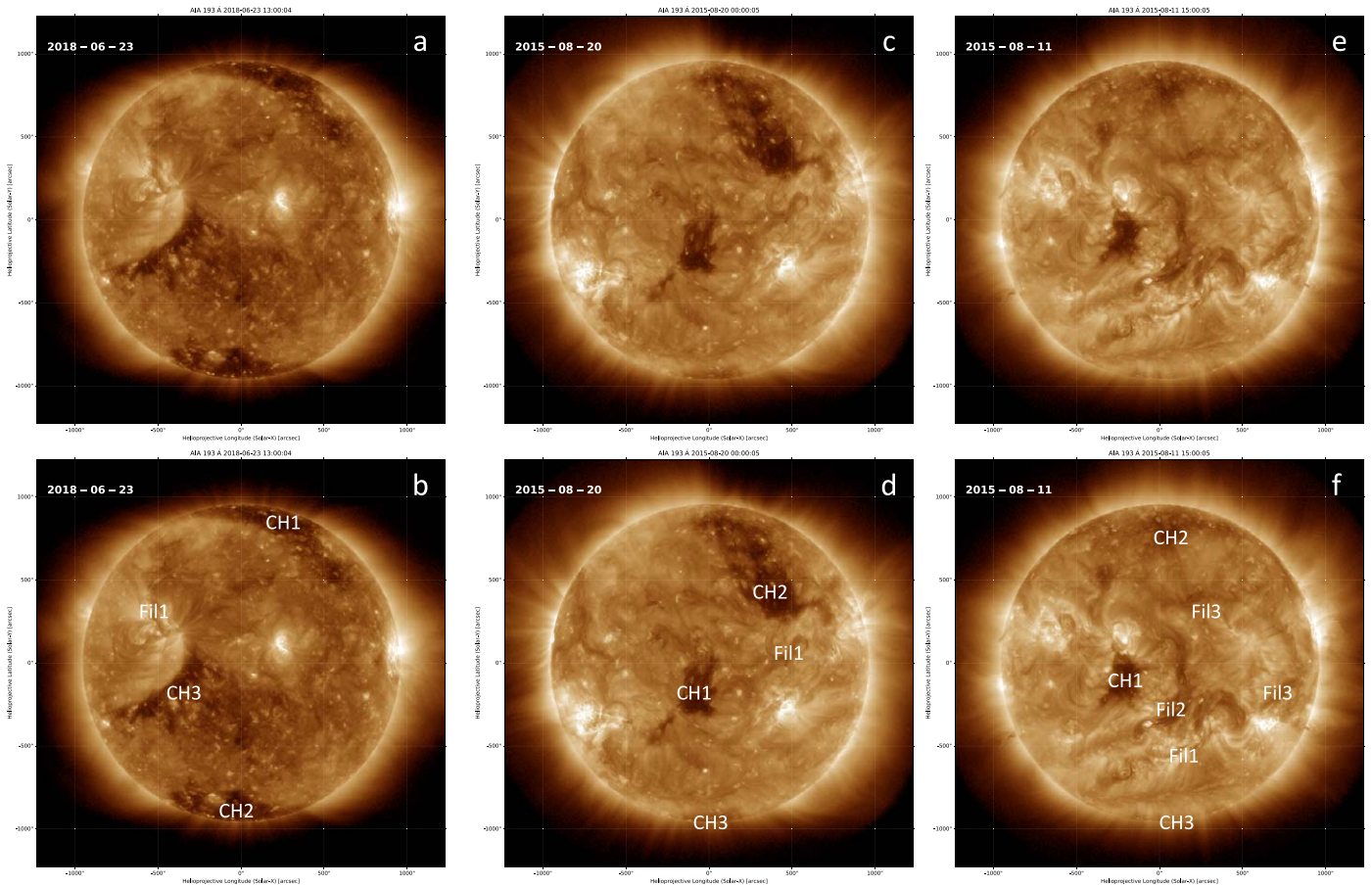
binary image of the Sun, with 1 representing pixels that the algorithm identifies as coronal holes and 0 representing noncoronal hole pixels. Panel (a) shows the number of overlapping coronal hole detections, with red indicating the largest overlap (15) and blue indicating the least overlap (0). Panels (b) and (c) display an AIA 193 Å image and an HMI magnetogram, with the largest (CNN193) and smallest (SPoCA-CH) detected coronal hole areas overlaid.

Following the definitions in Reiss et al. (2021), we calculated the physical properties of this coronal hole and compared the results obtained from the different schemes. Panels (d)–(i) show the coronal hole area, average AIA 193 Å intensity, signed and unsigned average magnetic flux density, and open magnetic flux. Additionally, the degree of unipolarity ( $U$ ) is calculated according to the definition provided by Ko et al. (2014) and Reiss et al. (2021). In this definition, a value of  $U$  equal to 0 indicates a pure unipolar field, while a value of  $U$  equal to 1 represents a pure bipolar magnetic field. Except from SPoCA-HEK, all automated schemes identify the coronal hole, with areas varying from  $1.58 \times 10^3 \text{ Mm}^2$  to  $169.31 \times 10^3 \text{ Mm}^2$ . The ratio between the smallest and largest coronal hole areas is 107.16, which is significantly larger than the ratio of 4.5 found in Reiss et al. (2021). Other properties, such as the average AIA 193 Å intensity, have a ratio of

2.19 between the smallest and largest values, which is similar to the ratio of 2.4 reported by Reiss et al. (2021).

A more detailed statistical analysis is presented in Table 3. For all physical properties (area, average intensity, signed average field, unsigned average field, degree of unipolarity and open magnetic flux) we calculated the following statistical measures: median, standard deviation, relative standard deviation (RSD), median absolute deviation (MAD), lower quartile (Q1), upper quartile (Q3), minimum value (min), maximum value (max), and maximum-minimum ratio (MMR). The median values for area, average intensity, signed average field, unsigned average field, degree of unipolarity, and open magnetic flux are  $42,079.96 \text{ Mm}^2$ ,  $11.49 \text{ DN s}^{-1}$ ,  $-1.10 \text{ G}$ ,  $7.50 \text{ G}$ ,  $0.85$ , and  $-5.53 \times 10^{20} \text{ Mx}$  respectively. The standard deviations are  $64,654.14 \text{ Mm}^2$ ,  $3.28 \text{ DN s}^{-1}$ ,  $0.42 \text{ G}$ ,  $0.16 \text{ G}$ ,  $0.06$ , and  $2.51 \times 10^{20} \text{ Mx}$ , respectively. The RSD values indicate variations relative to the median and are most significant for the area (89.1%), open magnetic flux (47.15%), and signed average magnetic field (42.94%).

A natural question arises: Why is this particular example so challenging for automated schemes? Tracing the temporal evolution of this coronal hole, we find that it persisted for several prior solar rotations and became a mixture of patches of



**Figure 1.** Full-disk images observed by SDO/AIA 193 Å on 2018 June 23, 2015 August 20, and 2015 August 11. The top row shows the solar disk in the Fe XII (193 Å;  $T \approx 1.6$  MK) emission line, the bottom row is the same with coronal holes and filament channels annotated. These annotations are used in Table 5.

open and closed magnetic field regions. The intensity of the coronal hole increases from the east to the west toward the disk center, which further complicates the process of locating a coronal hole boundary. Interestingly, although large parts of the coronal hole have high intensities in the Fe XII emission line (leading to small detected coronal hole areas according to many schemes), it is nevertheless the source of solar wind speeds exceeding  $600 \text{ km s}^{-1}$  and causes mild geomagnetic storm activity.

This example illustrates two points. First, that the boundaries of coronal holes detected by different methods can vary significantly; and, second, that relying solely on automated means for locating coronal holes in space-weather forecasting can be misleading.

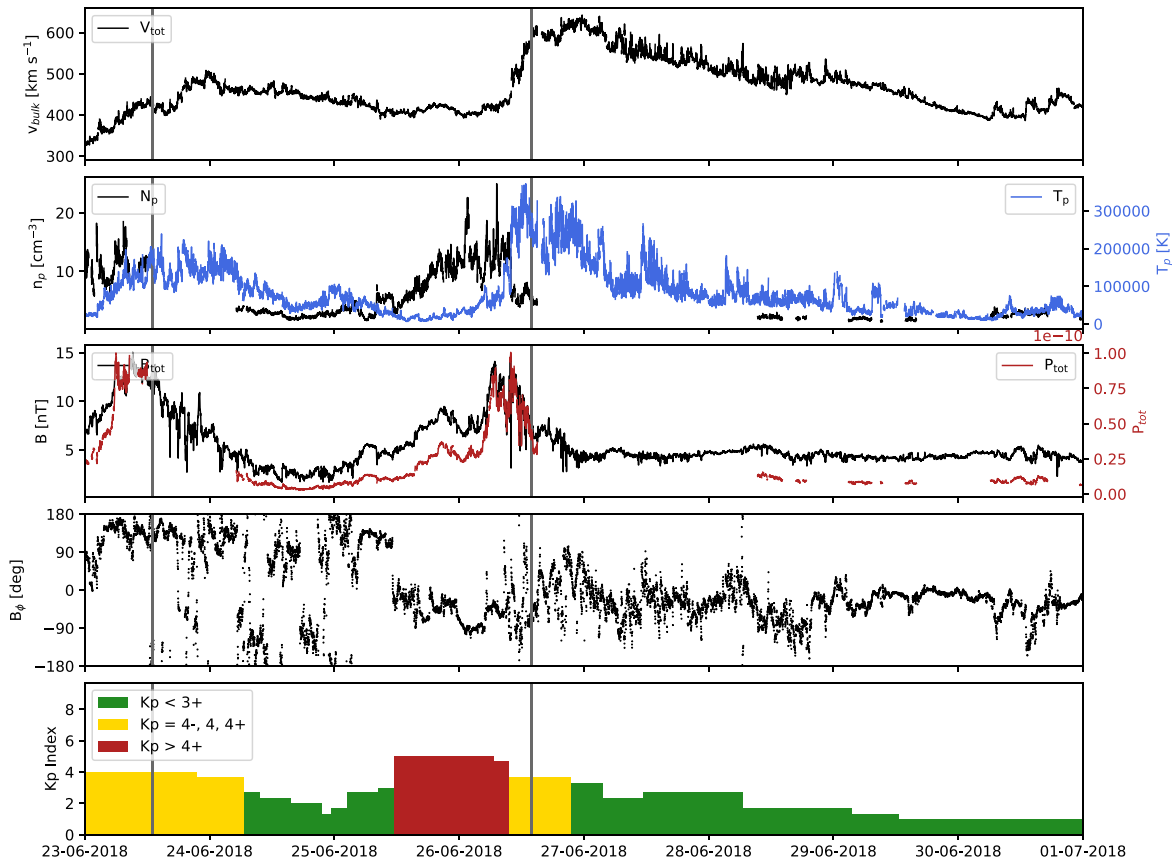
#### 4.2. Example II: 2015 August 20

The SDO image from our community data set on 2015 August 20 in Figure 6 shows the origin of another geomagnetic event. We identify the coronal hole at the disk center as a possible origin of a high-speed stream that arrived at Earth approximately 3 days later. By studying in situ measurements from the SWEPAM instrument aboard the ACE spacecraft in Figure 5, we find that the high-speed stream arrived at L1 with a maximum speed of  $570 \text{ km s}^{-1}$  on 2015 August 23, at approximately 08:00 UT. The geomagnetic storm started in the stream-interacting region before the arrival of the high-speed

stream, but there were no distinct signatures of an electron flux enhancement in the inner radiation belt.

Figure 6 shows the full-disk image under scrutiny observed by SDO/AIA 193 Å, with the coronal hole boundaries from different schemes overlaid. The most important features are two prevailing coronal holes; one located at the northern pole extending toward lower latitudes, and one close to disk center. Additionally, there is a small coronal hole at the south pole. The coronal hole boundaries from different schemes agree with each other, except for CHORTLE, which shows a significantly larger area. Some schemes detect the northern polar coronal hole and its low-latitude extension. A global dipole and an equatorial near-surface dipole often create such an extension to low latitudes (Timothy et al. 1975; Zirker 1977). Although relatively minor, the most significant differences originate from a dark patch located southeast of the equatorial coronal hole.

When looking at the same dark patch on 2015 August 18 (also included in the community data set), we see the patch is located east of the disk center. On 2015 August 18, all detection schemes besides CHRONNOS and SPoCA-CH identified the dark patch as a coronal hole. Interestingly, when we follow the evolution of the small patch over the next 2 days, we see an eruption in an active region close to the eastern limb. After the eruption, the newly formed open-field region merges with the small patch to create a large coronal hole, seen almost at disk center in Figure 6. Only six out of 15 automated schemes correctly identify the dark patch as a coronal hole on



**Figure 2.** In situ observations measured by ACE between 2018 June 23 and 2018 July 1. From top to bottom: bulk velocity (black, kilometers per second); proton density (black, cubic centimeters) and proton temperature (blue, kelvins), total magnetic field strength (black, nanoteslas) and total pressure (red), the angle of the magnetic field vector projected onto the  $x$ - $y$  plane,  $B_\phi$  (black, degrees), and  $Kp$  index where values less than 3+ are presented in green (quiet conditions), values 4-, 4, and 4+ in yellow (active conditions), and values greater than 4+ in red (storm conditions). Gray vertical lines represent the time at which the corresponding SDO image was taken (Figure 3), and the approximate high-speed stream arrival time.

2015 August 20, while 10 schemes correctly identify the southern polar coronal hole.

Figure 7(a) presents a detailed study of the coronal hole at the disk center following the approach outlined in the previous section. Panels (b) and (c) display an AIA 193 Å image and an HMI magnetogram, with the largest (CHORTLE) and smallest (SPoCA-CH) detected coronal hole areas overlaid. Panels (d) to (i) show the physical properties of this coronal hole, including the area, average AIA 193 Å intensity, signed and unsigned average magnetic flux density, degree of unipolarity, and open magnetic flux. The coronal hole area varies from  $20 \times 10^3$  Mm<sup>2</sup> to  $39 \times 10^3$  Mm<sup>2</sup>, except for the area found by CHORTLE, which is  $86 \times 10^3$  Mm<sup>2</sup>. The difference between the smallest and largest coronal hole areas is a factor of 1.91, excluding CHORTLE. When CHORTLE is included, the factor increases to 4.21, which is close to the 4.5 found in Reiss et al. (2021). Similarly, the average AIA 193 Å intensity has a factor of 1.49 when excluding CHORTLE; with CHORTLE, the factor is 2.24, compared to 2.4 in Reiss et al. (2021).

Table 4 shows a more detailed statistical analysis. The median values for the area, average AIA 193 Å intensity, signed average magnetic field, unsigned average magnetic flux density, degree of unipolarity, and open magnetic flux are 27,307.33 Mm<sup>2</sup>, 25.02 DN s<sup>-1</sup>, 2.74 G, 8.52 G, 0.68, and  $0.72 \times 10^{21}$  Mx, respectively. The standard deviations are 16,133.77 Mm<sup>2</sup>, 6.95 DN s<sup>-1</sup>, 0.36 G, 0.36 G, 0.03, and  $0.47 \times 10^{21}$  Mx. The RSD values are most significant for the

open magnetic flux (52.16%), area (49.92%), and average AIA 193 Å intensity (24.87%).

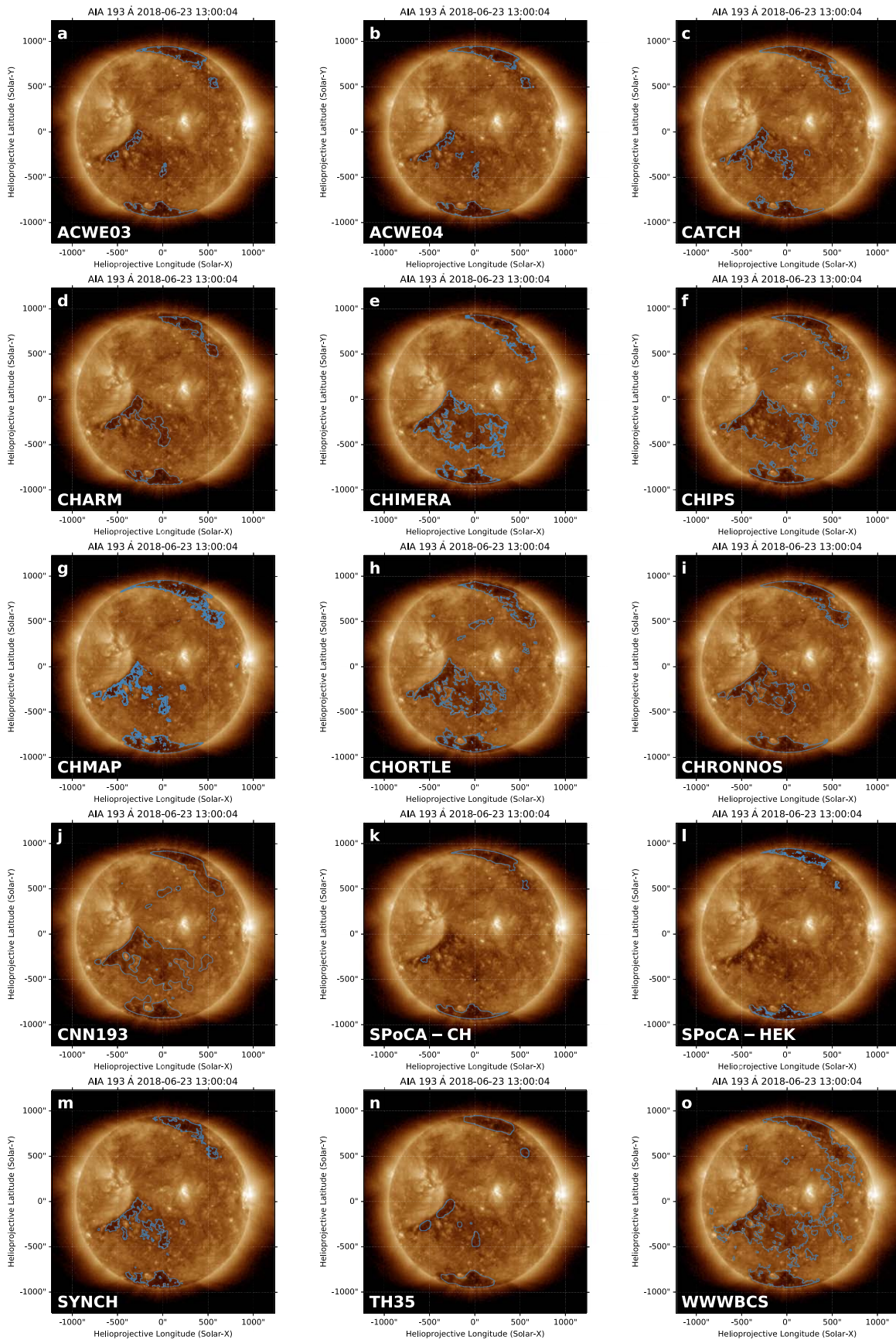
In contrast to the 2018 June 23 coronal hole in Section 4.1, the differences between the various schemes in this example are relatively small, with the most significant differences coming from a small patch southeast of the coronal hole.

#### 4.3. Example III: 2015 August 11

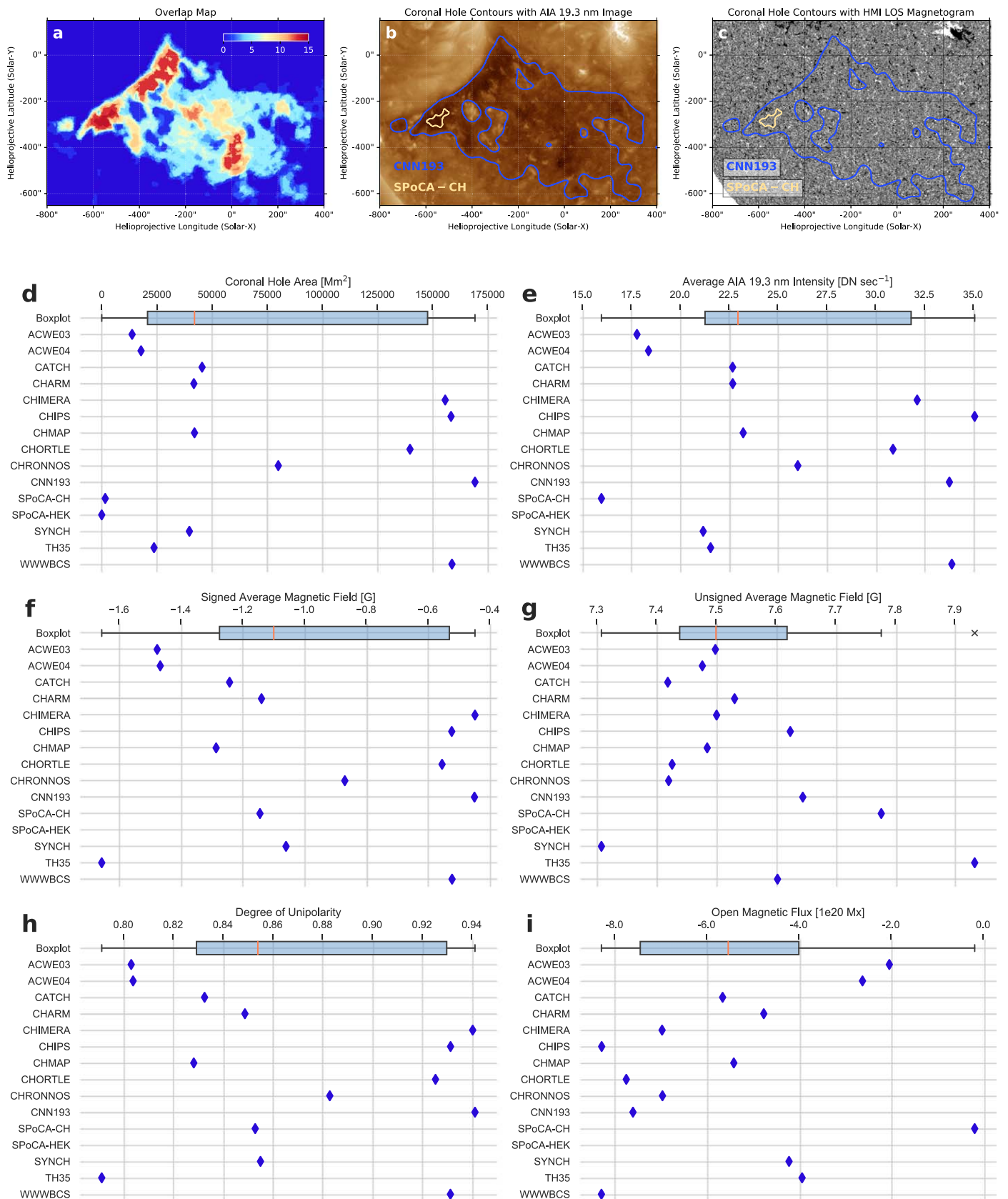
The final example of the community data set from 2015 August 11 demonstrates how the agreement between the schemes can look much worse. This is due to the difficulty of distinguishing coronal holes from filaments and quiet-Sun regions, which both can appear as dark regions in AIA EUV images.

According to current knowledge, the differentiation between filaments and coronal holes should be straightforward because filaments are closed magnetic structures and coronal holes have open fields that extend into space. Therefore, apart from H $\alpha$  images, the main distinguishing feature between the two is the distribution of the underlying photospheric magnetic field. The magnetic polarities around the filament area are largely balanced such that the integral of the LOS field over the area of the filament is zero or close to zero, even when inaccuracies in the field measurements and the boundaries of the filament are taken into account. The magnetic field of coronal holes is highly unbalanced, with an excess of one polarity extending into the heliosphere. However, previous research has shown





**Figure 3.** Full-disk image observed by SDO/AIA 193 Å, which is dominated by the Fe XII line emissions at a formation temperature of approximately 1.6 MK, on 2018 June 23. Panels (a)–(o) show the coronal hole boundary results for different automated detection schemes. Table 1 presents the wave bands needed as input for the corresponding automated detection scheme.



**Figure 4.** A comparison of the coronal hole maps of the equatorial coronal hole (CH3 in Figure 1; 2018 June 23) from the 15 different automated detection schemes. Top row: (a) number of overlapping coronal hole detections; (b) coronal hole contours overlaid on an AIA 193 Å image; (c) the same contours overlaid on an HMI LOS magnetogram saturated at  $\pm 30$  G. Rows 2–4: range of physical properties due to the choice of the detection scheme. (d) Coronal hole areas; (e) average AIA intensity in the 193 Å wave band; (f) signed average magnetic field strength; (g) unsigned average magnetic field strength; (h) degree of unipolarity; (i) open magnetic flux. On each boxplot, the central mark represents the median (50th percentile), while the edges of the box represent the 25th and 75th percentiles. The whiskers show the range of the data, excluding any outliers that are plotted individually.

**Table 3**  
Statistical Measures Summarizing the Results of 15 Different Automated Schemes for the Equatorial Coronal Hole Observed on 2018 June 23

Physical Property	Median	SD	RSD	MAD	Q1	Q3	Min	Max	MMR
Area (Mm <sup>2</sup> )	42,079.96	64,654.14	89.10%	56,933.13	20,778.75	147,820.11	0.00	169,313.63	...
Average intensity (DN s <sup>-1</sup> )	11.49	3.28	25.84%	2.82	10.65	15.92	7.99	17.54	2.19
Signed average field (G)	-1.10	0.42	42.94%	0.37	-1.27	-0.53	-1.66	-0.45	3.70
Unsigned average field (G)	7.50	0.16	2.14%	0.12	7.44	7.62	7.31	7.93	1.09
Degree of unipolarity	0.85	0.06	6.38%	0.05	0.83	0.93	0.79	0.94	1.19
Open magnetic flux (Mx)	$-5.53 \times 10^{20}$	$2.51 \times 10^{20}$	47.15%	$2.04 \times 10^{20}$	$-7.44 \times 10^{20}$	$-3.99 \times 10^{20}$	$-8.28 \times 10^{20}$	$-1.81 \times 10^{19}$	45.69

**Note.** The individual results for each automated scheme are compared in Figure 4. Abbreviations: standard deviation (SD), relative standard deviation (RSD), median absolute deviation (MAD), lower quartile (Q1), upper quartile (Q3), minimum value (Min), maximum value (Max), and maximum–minimum ratio (MMR).

that approximately 15% of all coronal hole candidates detected by automated means in SDO EUV imagery between 2011 and 2013 were filaments (Reiss et al. 2015). Automated schemes such as CHARM, CHIMERA, and CHRONNOS anticipate this issue by also using photospheric field measurements as input, but long-term quantitative studies are yet missing.

The SDO/AIA image from 2015 August 11 in Figure 8 shows a coronal hole at the northern pole and another well-defined coronal hole slightly east of the disk center. All the automated schemes detect the equatorial coronal hole, with only minor differences in the boundaries; however, a significant difference arises due to the presence of filaments. Solar plasma trapped at the tip of the helical winding of the filament is usually seen in H $\alpha$  images of the Sun. Figure 9 shows an H $\alpha$  image from the Big Bear Observatory. By examining an H $\alpha$  image and the temporal evolution of the structure, we can identify several filaments in this image. As discussed in the next section, most automated schemes erroneously identify at least some parts of these filaments as coronal holes. Exceptions are CATCH, where filaments have been removed by a human observer, and schemes that use a multiwavelength approach such as CHRONNOS and CHIMERA.

#### 4.4. Success and Failure in Assigning Labels in the Community Data Set

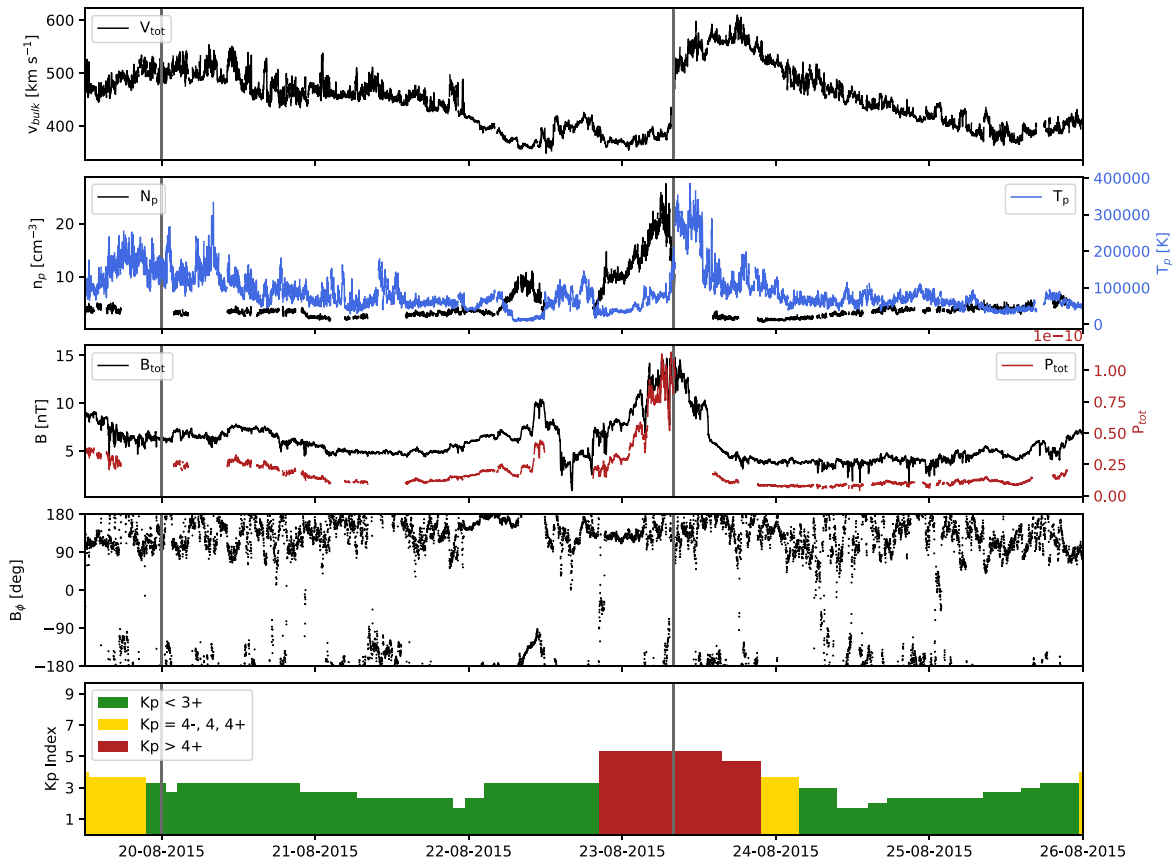
In this section, we will quantify the success of the automated detection schemes in assigning “coronal hole” labels in SDO images. There is no ground truth that tells us where to draw the line between open and closed magnetic field lines at a coronal hole boundary. In other words, any of the 15 coronal hole detections in the previous section could be a valid solution. However, an experienced observer can assess whether an automated scheme correctly labels a coronal hole region around an expected location. We use full-disk SDO images from the data set to visually assess where a coronal hole is likely to be located and assign a label to it. Since automated detection results can be contaminated by other structures such as filaments, as seen in Section 4.3, we also identify and label them in our data set. To identify filaments, we use H $\alpha$  images from the GONG network, AIA 304 Å, and 193 Å images, and track their evolution for 1–3 days.

Figure 1 illustrates the labeling process we used for the community data set for the SDO images on 2018 June 23, 2015 August 20, and 2015 August 11. The top row shows the AIA

193 Å images, and the bottom row shows the same images with coronal holes and filaments annotated. Our analysis does not take the size and shape of a region (coronal hole or filament) into consideration; thus, only a few pixels in the expected location are sufficient for a successful label. Table 5 shows the success or failure of the automated schemes in assigning labels to our three examples from the community data set. Note that CATCH is not included in this comparison as it does not operate without human interaction. A value of 1 indicates that the automated scheme has identified the structure, while 0 indicates that it has not. Ideally, the table shows all 1's in the coronal hole columns and all 0's in the filament columns, to match the detections of an experienced human observer.

We also add another column, called “QS?,” in Table 5. Automated schemes sometimes identify small clusters of pixels as coronal holes, although we assume these regions are part of the quiet Sun. We cannot rule out, however, that the identified pixels belong to a filament, which can sometimes be hard to identify, even for a trained human eye. The “QS?” column indicates whether the scheme has identified at least one cluster of pixels as a coronal hole (value of 1) or not (value of 0). Therefore, this column can be interpreted as representing the “thoroughness” of the automated scheme for the given SDO image. A value of 1 in the “QS?” column indicates that the automated scheme has overdetected structures in the SDO image. On 2018 June 23, we identify three coronal holes and one filament. All schemes, except SPoCA-HEK, correctly labeled all three coronal holes, and none of them misidentified the filament as a coronal hole. However, almost all of the schemes erroneously identified at least one cluster of pixels as a coronal hole, except for CHIMERA (see Figure 3). On 2015 August 20, all schemes identified CH1 and CH2, but CHARM, CHIMERA, CNN193, SYNCH, and TH35 missed CH3, likely due to its low-intensity contrast compared to the quiet Sun and its proximity to the south pole. Only CHORTLE erroneously labeled the filament as a coronal hole (see Figure 6). On 2015 August 11, we annotated three coronal holes and three filaments. All methods correctly identified CH1 and CH2, but only six out of 15 correctly labeled CH3, a small south pole coronal hole. While Fil1 was erroneously labeled as a coronal hole by CHORTLE and WWWBCS, Fil2 and Fil3 (an extended filament) were a challenge for almost all automated schemes. Only CHRONNOS managed to get all the labels correctly (see Figure 8).

Table 6 presents the statistics of categorical labels for the 29 SDO images in the community data set, in which we manually



**Figure 5.** In situ observations measured by ACE between 2015 August 19–26 in the same format as Figure 2.

labeled structures. For each of the detection schemes, we labeled the detected structures for all 29 images, with the exception of SPoCA-CH and SPoCA-HEK, which provided results for only 26 and 27 SDO images, respectively. These missing SDO images are due to SPoCA transitioning to quicklook images as the standard input for their detection schemes. As we want to use the same input data for all automated schemes we compare, we did not include these dates in this statistical analysis.

The manual labeling process for each of the algorithms involved labeling all detected regions and cross-checking with observations to determine true positives (TPs), false positives (FPs), false negatives (FNs), and true negatives (TNs). Table 6 shows the total number of coronal holes (#CHs) and filaments (#Fils), and the number of correctly labeled coronal holes (TPs), filaments labeled as coronal holes (FPs), coronal holes with missing labels (FNs), and filaments that were correctly rejected (TNs). The last two entries are the fractions of correctly labeled coronal holes among all coronal holes (TPR) and filaments incorrectly labeled as coronal holes out of all filaments (FPR).

Figure 10 shows the TPR and FPR for each detection scheme and illustrates that CHMAP correctly detected 98.8% of all observed coronal holes, WWWBCS 97.7%, and CHORTLE 91.9%. However, their fraction of erroneously labeled filaments were 49.3%, 38.0%, and 84.5%, respectively. Thus, a high success for coronal hole identification comes with a relatively high contamination with other structures. In contrast, CHIMERA has 0% filament identification rates, while SPoCA-CH has a 4% rate and ACWE03 has 7%. These automated schemes

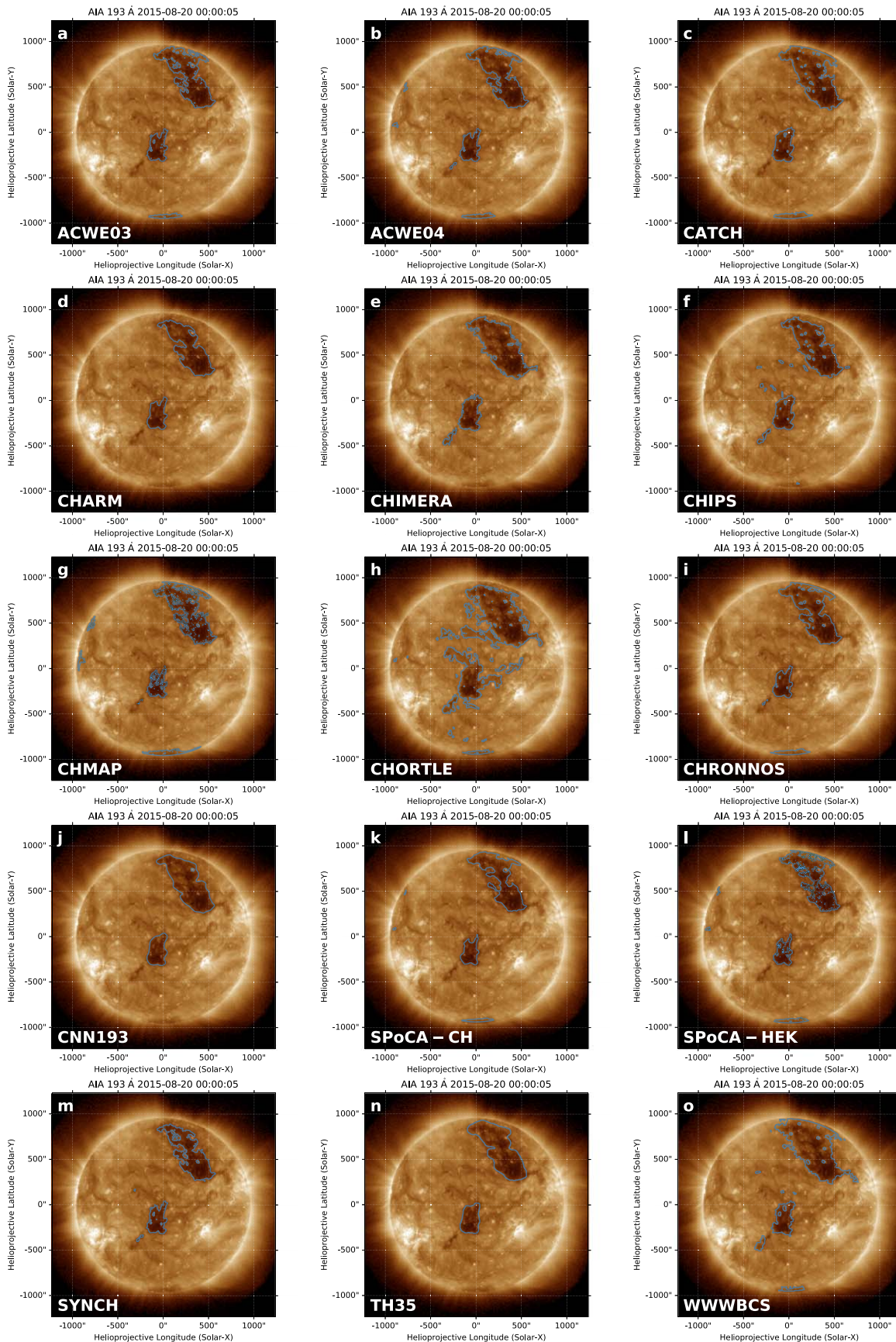
are less successful in coronal hole identification (78%, 84%, and 83%, respectively).

The CHIMERA method effectively avoids the erroneous detection of filaments as coronal holes through a multi-thermal segmentation approach, followed by a minimum area cutoff and a unipolarity check. As shown in Figure 6(c) in Garton et al. (2018), coronal hole segmentations obtained from the 211 Å and 171 Å passbands cut out almost all of the filament detections. The logical conjunction of the segmentations from the 211 Å and 171 Å passbands in Figure 7 of Garton et al. (2018) reveals that most, if not all, of the associated pixels from the filaments are removed. To further eliminate any remaining false positives, CHIMERA incorporates a minimum area cutoff and a unipolarity check. This ensures that smaller remnants of filaments are removed. A unipolarity check ensures that all detected coronal holes are sufficiently unipolar. The threshold for unipolarity in CHIMERA also depends on the size of the coronal holes (see Garton et al. 2018).

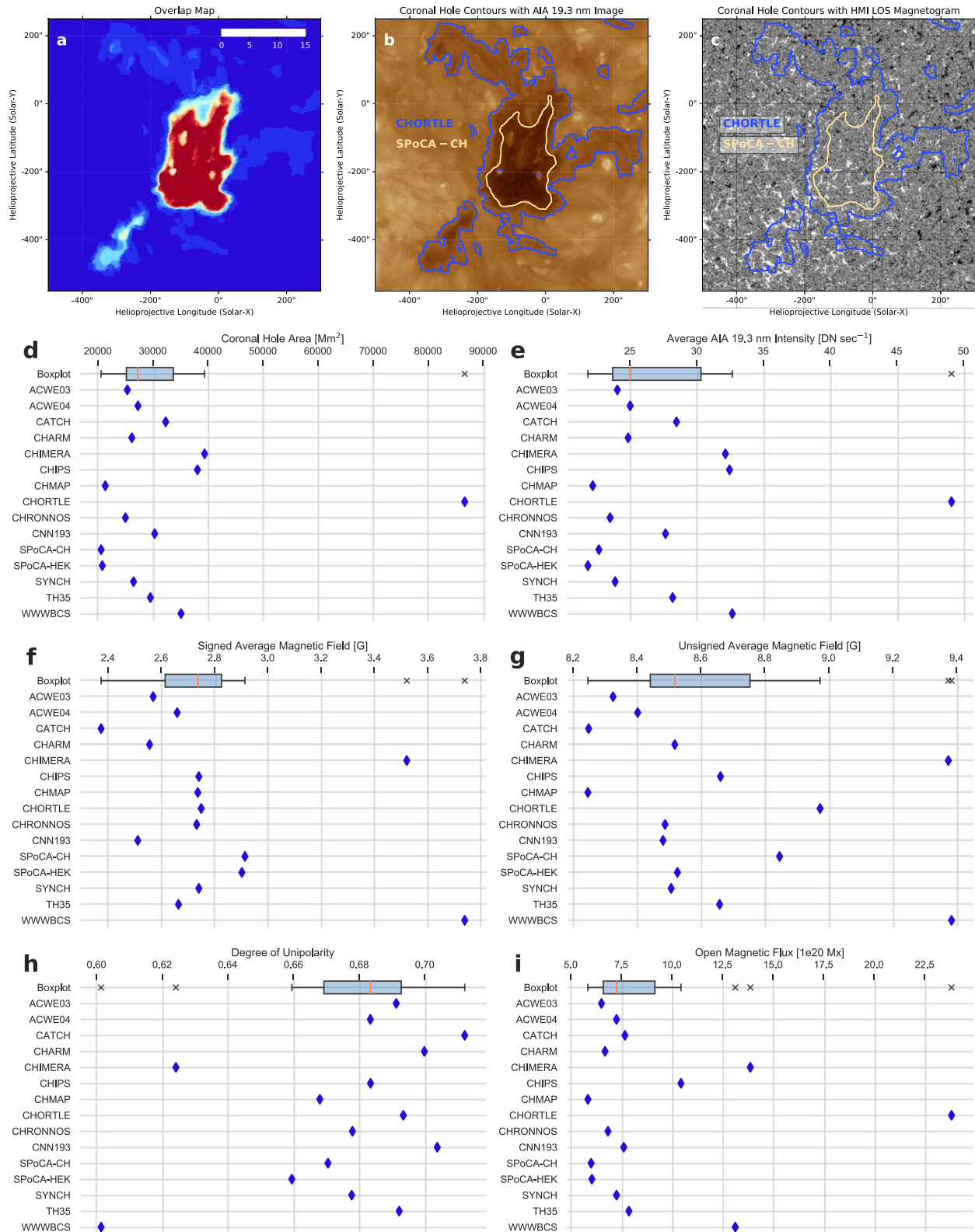
All identification tables and annotated SDO images are also available online in our community data set.

## 5. Discussion

The mission of the COSPAR ISWAT Coronal Hole Boundary Working Team (S2-01) is to answer the following questions: (1) How significant are the observational uncertainties of coronal hole boundaries in automated detection schemes? (2) To what extent does this uncertainty affect our phenomenological understanding of coronal holes and key science questions? (3) How can our activities support the research community in the long term? (4) How can these



**Figure 6.** Full-disk image observed by SDO/AIA 193 Å, which is dominated by the Fe XII line emissions at a formation temperature of approximately 1.6 MK, on 2015 August 20. Panels (a)–(o) show the coronal hole boundary results for different automated detection schemes widely applied in the community. Table 1 presents the wave bands needed as input for the corresponding automated detection scheme.



**Figure 7.** A comparison of the coronal hole maps of the equatorial coronal hole (CH1 in Figure 1; 2015 August 20) from the 15 different automated detection schemes: Top row: (a) number of overlapping coronal hole detections; (b) coronal hole contours overlaid on an AIA 193 Å image; (c) the same contours overlaid on an HMI LOS magnetogram saturated at  $\pm 30$  G. Rows 2–4: range of physical properties of CH1 due to the choice of the detection scheme. (d) Coronal hole areas; (e) average AIA intensity in the 193 Å wave band; (f) signed average magnetic field strength; (g) unsigned average magnetic field strength; (h) degree of unipolarity; (i) open magnetic flux. On each boxplot, the central mark represents the median (50th percentile), while the edges of the box represent the 25th and 75th percentiles. The whiskers show the range of the data, excluding any outliers that are plotted individually.

**Table 4**  
Statistical Measures Summarizing the Results of 15 Different Automated Schemes for the Equatorial Coronal Hole Observed on 2015 August 20

Physical Property	Median	SD	RSD	MAD	Q1	Q3	Min	Max	MMR
Area (Mm <sup>2</sup> )	27,307.33	16,133.77	49.92 %	9344.59	25,199.78	33,739.62	20,609.64	86,667.31	4.21
Average intensity (DN s <sup>-1</sup> )	25.02	6.95	24.87 %	4.74	23.71	30.33	21.86	49.11	2.25
Signed average field (G)	2.74	0.36	12.98 %	0.25	2.62	2.83	2.37	3.74	1.58
Unsigned average field (G)	8.52	0.36	4.15 %	0.27	8.44	8.75	8.25	9.38	1.14
Degree of unipolarity	0.68	0.03	4.36 %	0.02	0.67	0.69	0.60	0.71	1.18
Open magnetic flux (Mx)	$0.72 \times 10^{21}$	$0.47 \times 10^{21}$	52.16 %	$0.33 \times 10^{21}$	$0.66 \times 10^{21}$	$0.92 \times 10^{21}$	$0.59 \times 10^{21}$	$2.38 \times 10^{21}$	4.08

**Note.** Abbreviations: standard deviation (SD), relative standard deviation (RSD), median absolute deviation (MAD), lower quartile (Q1), upper quartile (Q3), minimum value (Min), maximum value (Max), and maximum-minimum ratio (MMR).

findings enhance our space-weather modeling assets? In the following, we will discuss how this study contributes to the first three questions and the existing literature.

### 5.1. How Significant Are the Observational Uncertainties of Coronal Hole Boundaries in Automated Detection Schemes?

To answer this question quantitatively, Reiss et al. (2021) compared the coronal hole boundary detections of nine automated schemes. In this previous study, we focused on an equatorial coronal hole observed by SDO on 2018 May 30, which is included in the community data set. We showed that the choice of the detection scheme can significantly change the location of coronal hole boundaries and the physical properties computed in the coronal hole region. Properties such as the area, mean EUV intensity, and average magnetic field strength varied by a factor of up to 4.5 between schemes. A pending question is whether the derived uncertainties represent a general trend.

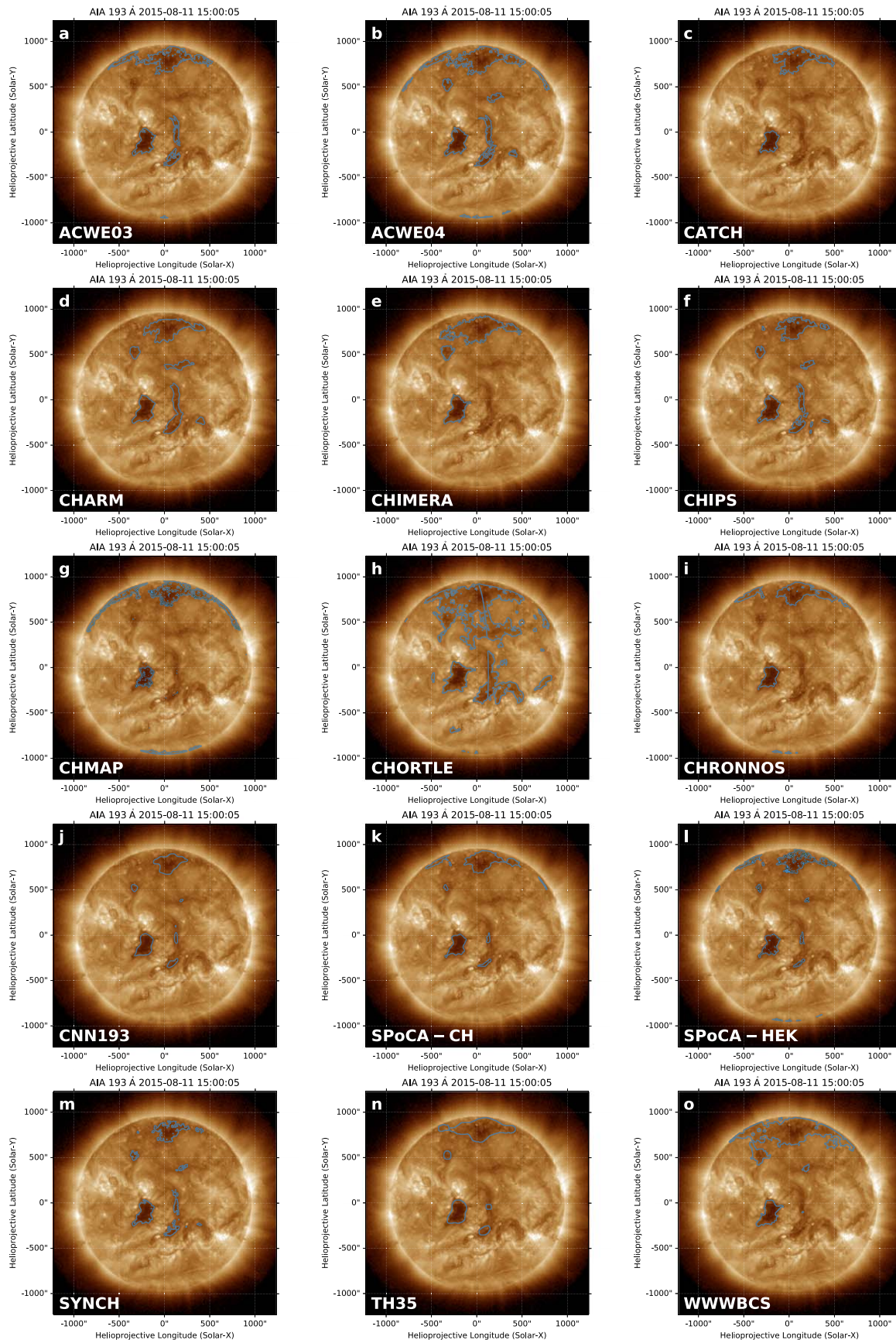
This study expands our work in Reiss et al. (2021) in several ways. First, we selected 29 full-disk images from the SDO data repository to challenge automated coronal hole detection schemes. Second, we collaborated with the coronal hole research community worldwide via the COSPAR ISWAT initiative and collected the results of 15 automated coronal hole detection schemes. Third, we combined the SDO images and the coronal hole detection results in a community data set. By making this community data set available and citable via doi:10.6084/m9.figshare.23997993.v1, we envisage that the data set will provide the community with a point of reference for improving existing and developing future schemes. Fourth, we used three SDO images from this community data set to outline lessons learned on this journey, and conducted a comprehensive statistical analysis by manually labeling coronal holes and filaments and cross-checking the results.

We find that detection results for the equatorial coronal hole observed by the SDO spacecraft on 2018 June 23 differed significantly among the automated detection schemes. The coronal hole (CH3 in Figure 1(b)) persisted over multiple Carrington rotations, and its mixed polarity contribution would be expected to increase, making the region appear brighter in EUV emission as it evolved. Overarching bright loops from the adjacent active region partially obscured the coronal hole (Wang 2017). Besides SPoCA-CH and SPoCA-HEK, all the detection schemes agreed near the active region due to the stark intensity contrast. Further away from the active region, the detection results varied significantly. Nevertheless, the existence of the coronal hole was accompanied by the arrival of a high-speed stream at L1 on 2018 June 26 with a significant bulk speed of  $600 \text{ km s}^{-1}$ .

The choice of the automated scheme had an even greater effect on 2018 June 23 than our initial findings for an image on 2018 May 30 in Reiss et al. (2021). While all automated schemes besides SPoCA-HEK located the coronal holes, the area varies from  $1.58 \times 10^3 \text{ Mm}^2$  to  $169.31 \times 10^3 \text{ Mm}^2$ . This corresponds to a ratio between the smallest and largest coronal hole areas of 107.16, which is much larger than the 4.5 reported by Reiss et al. (2021). However, other properties such as the average AIA 193 Å intensity have a ratio of 2.19 between the smallest and largest values, which is similar to the ratio of 2.4 reported by Reiss et al. (2021). The effect that the choice of the detection scheme has depends on the individual image assessed. This also means that the study of an individual coronal hole does not necessarily provide a guideline of the uncertainty that can be expected when another SDO image is studied. We therefore do not recommend using the uncertainties presented in this study as a general guideline. It should rather raise awareness that relying on automated schemes might lead to misleading results and that additional research is needed, for example by studying multiple coronal holes over an extended period of time.

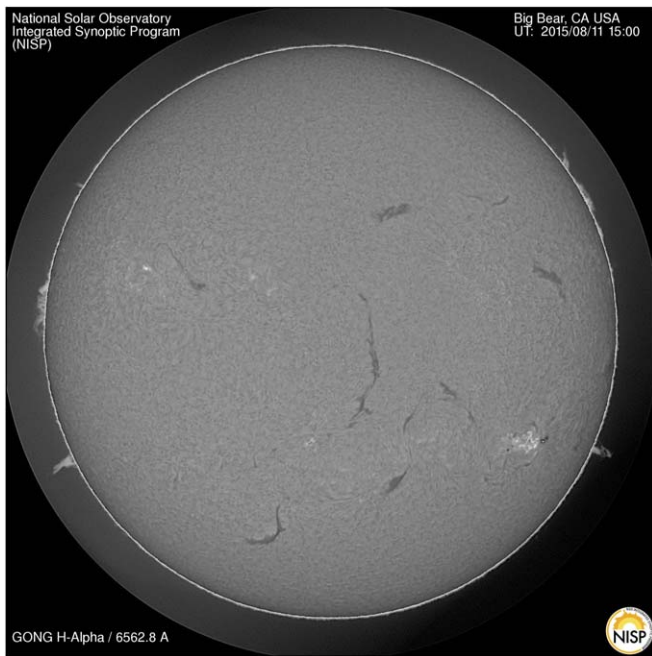
We find that the detection results are quite consistent for the coronal hole (CH1 in Figure 1(d)) observed by the SDO spacecraft on 2015 August 20. In this example, most differences come from a small dark patch located southeast of the coronal hole. Overall, the coronal hole areas from the different schemes vary between  $20 \times 10^3 \text{ Mm}^2$  to  $39 \times 10^3 \text{ Mm}^2$ , except for CHORTLE, which is  $86 \times 10^3 \text{ Mm}^2$ . The difference between the smallest and largest coronal hole areas is a factor of 1.91, excluding CHORTLE. When CHORTLE is included, the factor increases to 4.21, which is close to the 4.5 found in Reiss et al. (2021). Similarly, the average AIA 193 Å intensity has a factor of 1.49 when excluding CHORTLE; with CHORTLE, the factor is 2.24, compared to 2.4 in Reiss et al. (2021). We note that a newer version of CHORTLE has been developed that might alleviate some of the issues seen in the present study. The agreement between the schemes in this example is reasonable; however, when studying the SDO image just several days earlier, on 2015 August 11, we see a significantly different situation once again.

Our analysis of the SDO image observed on 2015 August 11 shows that further research is needed to differentiate between coronal holes and filaments. This challenge has been addressed before in Reiss et al. (2015). By labeling coronal hole candidates observed in all the SDO images between the years 2015 to 2018, Reiss et al. (2015) found that approximately 15% of the coronal hole candidates were filaments. Several detection schemes have built-in classification rules for testing all the coronal hole candidates. For instance, Krista & Gallagher (2009) use the



**Figure 8.** Full-disk image observed by SDO/AIA 193 Å, which is dominated by the Fe XII line emissions at a formation temperature of approximately 1.6 MK, on 2015 August 11. Panels (a)–(o) show the coronal hole boundary results for different automated detection schemes widely applied in the community. Table 1 presents the wave bands needed as input for the corresponding automated detection scheme.





**Figure 9.**  $H\alpha$  image observed by the Big Bear Observatory on 2015 August 11.

skewness of the magnetic field strength distribution to delineate coronal holes from filaments.

A promising avenue for filament removal is cross-checking coronal hole candidates with  $H\alpha$  images, as shown in Figure 9. Filament channels have a magnetic field that is dominated by the axial component. Cool coronal plasma sitting in the dip of the helical windings can be seen as dark regions in  $H\alpha$  images. However, filament channels are sometimes only partly, or not at all, filled with plasma material. Hence, not all filaments show these clear signatures in  $H\alpha$ , and ground-based observations are not always available.

An additional strategy is to look into multiple wave bands simultaneously. Detection schemes that use multiple wave bands simultaneously provide the most promising results. Intuitively, this makes sense because the AIA wave bands 171 Å and 304 Å show plasma inside filament channels, albeit higher up in the corona and, therefore, as larger regions than in  $H\alpha$ . Automated schemes based on data science, such as CHRONNOS and CNN193, have learned this rule by training on manually labeled data sets. We note that the results from 2015 August 11 are characteristic of the results for other SDO images in the community data set that we selected to investigate this question.

Besides this study and our work in Reiss et al. (2021), the observational uncertainties of coronal hole boundaries have been investigated by Linker et al. (2021). The authors studied a coronal hole observed by SDO on 2010 September 19 to scrutinize whether differences in the automated schemes can account for the missing open flux in observations. Linker et al. (2021) concluded that the uncertainty might contribute to the underdetection of open flux but are unlikely to solve the open flux problem (Linker et al. 2017).

To reiterate, we have studied the question of how significant the observational uncertainties of coronal hole boundaries are in automated detection schemes for three examples. While this is an important first step, we also find that the results can vary significantly depending on the SDO image being examined.

Therefore, further research should focus on coronal holes over an extended period of time, rather than focusing on single SDO images.

### 5.2. To What Extent Does This Uncertainty Affect Our Phenomenological Understanding of Coronal Holes and Key Science Questions?

Understanding the uncertainties that result from automated detection schemes is vital for addressing critical questions in solar and heliospheric science (Viall & Borovsky 2020; Reiss et al. 2023). Our findings most directly feed into research on the life cycle of coronal holes and their relation to the evolving solar wind flows and embedded magnetic fields (Wang et al. 2010; de Toma 2011; Ko et al. 2014; Krista et al. 2018). Many studies have related the physical properties of coronal holes deduced from automated schemes with the solar wind conditions at Earth (Nolte et al. 1976; Robbins et al. 2006; Vršnak et al. 2007; Rotter et al. 2012; Reiss et al. 2016; Garton et al. 2018). Our results indicate that the choice of the detection scheme might significantly affect the coronal hole locations. Thus far, these uncertainties have not been taken into consideration. Our findings also support recent efforts to construct error boundaries as an inherent output of automated schemes (Heinemann et al. 2019).

Previous research has been devoted to understanding the global distribution of coronal holes during the solar cycle (Lowder et al. 2017). In particular, tracing coronal holes and computing their open magnetic flux is an essential diagnostic of the solar activity cycle (Harvey & Recely 2002; Wang 2009). A promising research avenue would be to expand our analysis over an extended time, tracing the temporal and spatial evolution of coronal holes. The effect that the wavelength of the EUV image, the position of the coronal hole on the solar disk, and the phase in the solar cycle have on the coronal hole boundaries are of most interest.

We outline research questions that might benefit from such an analysis in the COSPAR ISWAT roadmap paper prepared by Cluster S2 in Reiss et al. (2023). Examples include the effect of automated detection schemes on the open flux problem (Linker et al. 2017, 2021), coronal holes as an observational test for the accuracy of magnetic models of the corona (Mackay et al. 2002; Yeates et al. 2010), and the validation of magnetic connectivity tools (S2-05). Quantifying the uncertainties in coronal hole boundaries will provide a critical observational test for magnetic models of the corona that are the cornerstone of many space-weather research and forecast models. Such models are operational at NOAA in the United States, the Met Office in the United Kingdom, and other forecasting agencies.

Since the SDO images in the community data set were selected to challenge automated schemes, we do not state here that uncertainties such as those found for 2018 June 23 should serve the community as a general guideline. Nevertheless, these uncertainties, along with the high rate of contamination with other solar structures such as filaments, are alarming. The current analysis cannot answer how possible errors in coronal hole detection have affected our current understanding of this solar phenomenon, but it does show that this question is justified.

**Table 5**  
Statistics of Coronal Hole and Filaments Labels for the SDO Images Recorded on 2018 June 23, 2015 August 20, and 2015 August 11 (see Figure 1)

Model	Event 1: 2018 June 23					Event 2: 2015 August 20					Event 3: 2015 August 11						
	CH1	CH2	CH3	Fil1	QS?	CH1	CH2	CH3	Fil1	QS?	CH1	CH2	CH3	Fil1	Fil2	Fil3	QS?
ACWE03	1	1	1	0	1	1	1	1	0	0	1	1	1	0	1	0	0
ACWE04	1	1	1	0	1	1	1	1	0	1	1	1	1	0	1	1	1
CHARM	1	1	1	0	1	1	1	0	0	0	1	1	0	0	1	1	1
CHIMERA	1	1	1	0	0	1	1	0	0	1	1	1	0	0	0	0	1
CHIPS	1	1	1	0	1	1	1	1	0	1	1	1	0	0	1	1	1
CHMAP	1	1	1	0	1	1	1	1	0	1	1	1	1	0	1	0	1
CHORTLE	1	1	1	0	1	1	1	1	1	1	1	1	1	1	1	1	1
CHRONNOS	1	1	1	0	1	1	1	1	0	1	1	1	1	0	0	0	1
CNN193	1	1	1	0	1	1	1	0	0	0	1	1	1	0	0	1	1
SPoCA-CH	1	1	1	0	1	1	1	1	0	1	1	1	0	0	1	0	1
SPoCA-HEK	1	1	0	0	1	1	1	1	0	1	1	1	0	1	1	1	1
SYNCH	1	1	1	0	1	1	1	0	0	1	1	1	0	0	1	1	1
TH35	1	1	1	0	1	1	1	0	0	0	1	1	0	0	1	0	1
WWWBCS	1	1	1	0	1	1	1	1	0	1	1	1	0	1	1	1	0

**Notes.** The value 1 indicates that the automated scheme has correctly labeled the structure, and 0 indicates that it did not. In contrast, the “QS?” column indicates whether the automated scheme has identified at least one cluster of quiet-Sun pixels as a coronal hole (value of 1) or not (value of 0). It can be interpreted as an overall measure of the “thoroughness” of the corresponding scheme in this image. Abbreviations: coronal hole (CH) and filament (Fil).

**Table 6**  
Statistical Analysis of Categorical Labels for the Community Data Set

Model	#CHs	#Fils	TP	FP	FN	TN	TPR	FPR
ACWE03	86	71	71	5	15	66	0.83	0.07
ACWE04	86	71	74	21	12	50	0.86	0.29
CHARM	86	71	68	15	18	56	0.79	0.21
CHIMERA	86	71	67	0	19	71	0.78	0
CHIPS	86	71	74	38	12	33	0.86	0.54
CHMAP	86	71	85	35	1	36	0.99	0.49
CHORTLE	86	71	79	60	7	11	0.92	0.85
CRONNOS	86	71	73	9	13	62	0.85	0.13
CNN193	86	71	70	25	16	46	0.82	0.35
SPoCA-CH	76	70	64	3	12	67	0.84	0.04
SPoCA-HEK	80	71	70	18	10	53	0.87	0.25
SYNCH	86	71	75	44	11	27	0.87	0.62
TH35	86	71	66	15	20	56	0.77	0.21
WWWBCS	86	71	84	27	2	44	0.98	0.38

**Notes.** The last two entries are the fractions of correctly labeled coronal holes among all coronal holes (TPR) and filaments incorrectly labeled as coronal holes out of all filaments (FPR). Abbreviations: true positives (TP), false positives (FP), false negatives (FN), true negatives (TN), true positive rate (TPR), and false positive rate (FPR).

### 5.3. How Can Our Activities Support the Research Community in the Long Term?

Since establishing the COSPAR ISWAT Coronal Hole Boundary Working Team, we have organized regular meetings to tie together the coronal hole research community. One of the discussion outcomes was that common ground is needed for comparative studies. We envisage that the community data set will serve the solar and heliospheric science community as an unbiased reference for improving existing and developing new detection schemes.

To make the best use of this community data set, we recommend using the data set as a holdout data set for comparisons in the final stage of new developments. In this way, the detection results are not optimized for the community data set and give a more realistic insight into the abilities of the new schemes and a fair comparison to existing schemes. We

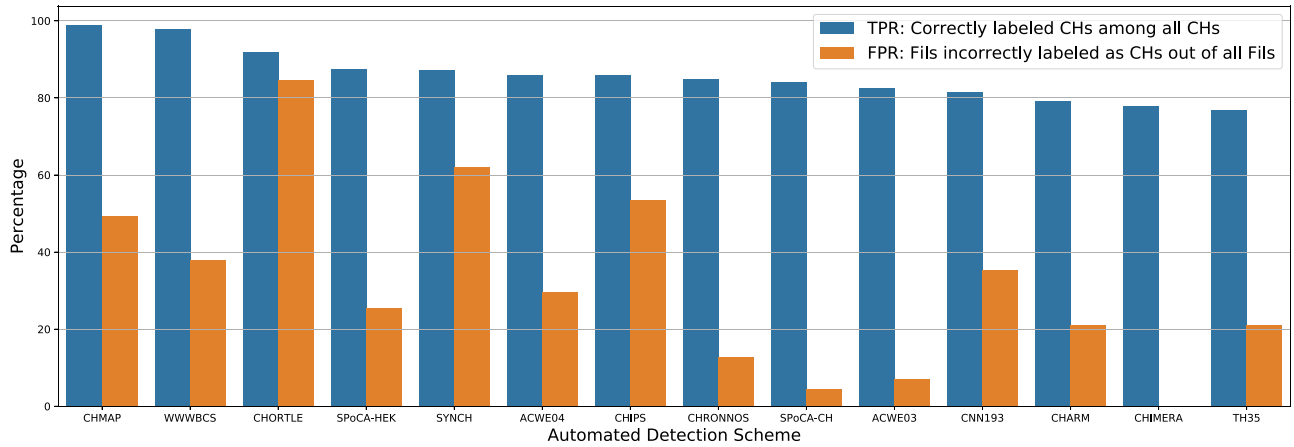
also note that corrections, as detailed in Section 3, have been applied to all the SDO images in the data set. We used these SDO images as input for all the detection schemes in this study to remove uncertainties caused by different preprocessing steps. Therefore, we recommend using the SDO images as provided in the community data set in possible future comparisons.

By keeping the data set up to date with newly developed detection schemes and versions thereof, we envisage that the data set will provide a helpful reference for automated coronal hole detection in the long term. The community data set alongside the coronal hole detection results are available online at doi:[10.6084/m9.figshare.23997993.v1](https://doi.org/10.6084/m9.figshare.23997993.v1).

## 6. Summary

The standard approach for locating coronal hole boundaries in observations from the SDO relies on automated detection schemes. While many automated schemes have been developed in the SDO era, a quantitative comparison between different schemes has received, if at all, scant attention until recently. Therefore, the uncertainties associated with the choice of the detection scheme for locating coronal holes in SDO imagery are unknown. We surmise that this shortcoming is partly due to a lack of data agreed upon by the community for comparison. This study presents the first community data set for comparing automated coronal hole detection schemes. The data set includes 29 SDO images with the purpose of challenging automated schemes. By tying together the expertise in coronal hole research worldwide, the data set also contains the coronal hole masks of the most widely applied detection schemes. We envisage that this community data set will serve the solar and heliospheric science community as a point of reference for evaluating existing detection schemes and developing future ones.

We illustrate some lessons learned using three SDO images from the community data set. First, the SDO image in the catalog from 2018 June 23 shows that an equatorial coronal hole, which was responsible for moderate geomagnetic storm activity, is not detected by all automated schemes. These results indicate that the choice of the detection scheme can



**Figure 10.** Comparison of the fraction of correctly labeled coronal holes among all coronal holes (TPR, blue) and fraction of filaments incorrectly labeled as coronal holes out of all filaments (FPR, orange). CATCH is not included in this comparison as it does not operate without human interaction.

significantly affect the size and shape of coronal hole boundaries, in line with our previous findings in Reiss et al. (2021). Second, the example on 2015 August 20 shows that coronal hole boundaries computed from different schemes can also agree reasonably well on a large scale, depending on the global coronal magnetic field structure. Third, the SDO image on 2015 August 11 shows that almost all automated schemes under scrutiny are prone to confusing coronal holes with filaments, which is a significant problem for studying the long-term evolution of coronal holes with automated schemes. Finally, we quantify the ability of automated detection schemes in assigning “coronal holes” labels to all SDO images in our community data set. We find that a high success rate for coronal hole identifications is usually accompanied by an increased probability of detecting other structures, such as filaments and quiet-Sun regions. We envision that the community catalog, along with the analysis performed in this study, will be the starting point for more rigorous comparisons of automated detection schemes.

### Acknowledgments

The authors thank all contributors to the COSPAR ISWAT initiative, which supported this research effort. This research was funded in part by the Austrian Science Fund (FWF) [P34437, J4160-N27, and P31659]. For the purpose of open access, the author has applied a CC BY public copyright licence to any Author Accepted Manuscript version arising from this submission. The authors thank the following organizations and programs: C.M. and E.E.D. are funded by the European Union (ERC, HELIO4CAST, 101042188). Views and opinions expressed are, however, those of the author(s) only and do not necessarily reflect those of the European Union or the European Research Council Executive Agency. Neither the European Union nor the granting authority can be held responsible for them. K.M. acknowledges support by the NASA HGI program (grant No. 80HQTR19T0028), the NASA cooperative agreement NNG11PL10A and grant No. 80NSSC21M0180, and support from the NASA Living With a Star program through its Heliospheric Science Support Office. We acknowledge the Community Coordinated Modeling Center (CCMC) at Goddard Space Flight Center for the use of iSWA (<https://ccmc.gsfc.nasa.gov/tools/iSWA/>). The authors would like to express their gratitude to the anonymous reviewer for the valuable and constructive criticism.

### Appendix A

#### ACWE: Active Contours without Edges

The ACWE algorithm, from Boucheron et al. (2016), has been translated from MATLAB to Python, and is discussed in detail in Grajeda et al. (2023). Following the implementation in Boucheron et al. (2016), EUV 193 Å observations are spatially downsampled to  $512 \times 512$  pixel resolution, then corrected for limb brightening. From these images the on-disk area is extracted and a histogram of on-disk intensities is generated. The mean intensity of the quiet Sun (QS) is estimated from the histogram as the intensity of the bin with the most pixels. The initial contour is then defined as all regions with an intensity  $\leq \alpha \times QS$ , where  $\alpha$  is a user-defined parameter. Results for an initial seed generated with  $\alpha = 0.3$  (designated ACWE03) and  $\alpha = 0.4$  (designated ACWE04) are both provided. Prior to performing ACWE, a morphological hole-filling operation is performed to eliminate holes within the initial seed, and off-disk areas of the downsampled and corrected EUV images are masked from the algorithm by setting the intensity of this region to the mean intensity of the non-coronal-hole (non-CH) region. ACWE is then performed with a contour length constraint  $\mu = 0$ , a foreground (CH) homogeneity parameter  $\lambda_i = 1$ , and a background (non-CH) homogeneity parameter  $\lambda_o = 1/50$ . Every 10 iterations, until convergence, the intensity of the off-disk region is reset to the mean intensity of the non-CH regions. Changes between ACWE in Boucheron et al. (2016) and the algorithm as implemented here consist of the implementation in Python, the choice of homogeneity parameters  $\lambda_i = 1$  and  $\lambda_o = 1/50$  (which matches the choice of parameters in Section 4 of Boucheron et al. 2016), and the use of seeding parameters  $\alpha = 0.3$  and  $\alpha = 0.4$ .

### Appendix B

#### CHIPS: Coronal Hole Identification Using a Probabilistic Scheme

CHIPS is a probabilistic algorithm that can identify coronal holes and associated coronal hole boundaries from the solar full-disk and synoptic maps, taken in 171 Å, 193 Å, and 211 Å wave bands. The unique selling proposition of CHIPS is that this model provides probability ( $\theta$ ) against each of the identified coronal holes and associated coronal hole boundaries, which provides a measure of certainty about the detection mechanism. In addition, in one run it provides multiple coronal

holes and associated coronal hole boundaries from one image. The processing modules to detect coronal holes are shared between the different image types. The processing units primarily exploit knowledge from solar physics to segment coronal holes with different threshold values on the EUV image and then estimate coronal hole boundaries, which includes the image intensity within coronal holes being less than their neighboring pixels. This algorithm is tuned to operate best on SDO/AIA images.

The three major processes of the scheme are (i) filtering, (ii) threshold identification, and (iii) coronal hole identification. We describe the processing units in terms of SDO/AIA full-disk images that hold for synoptic maps also. Full-disk images are passed to the filtering unit, while EVU synoptic maps from the SDO database are filtered directly for later processing. The filtering units consist of two primary steps. First, filter the image using a two-dimensional Gaussian median filter with a user-defined kernel, to remove the speckle and noise in the image. Second, the module uses a user-defined sliding window to identify different regions which will be processed by subsequent processing units to extract intensity thresholds. For each region identified by the filtering unit, CHIPS extracts the optimal intensity of that region, which can identify darker coronal holes from neighboring brighter pixels, using Otsu's method. The assumption of using Otsu's method is that the intensity histogram for a pixel within a region is bimodal and possesses a sharp and deep valley between the two peaks. This region-based threshold identification provides several possible thresholds to identify coronal holes. In the final processing step, CHIPS uses threshold values to convert the grayscale EUV image to a binary image and identify coronal hole boundaries. For each intensity threshold value ( $I_{th}$ ), CHIPS estimates the probability of the identified regions being coronal holes by first transforming the pixel intensities into probability space by subtracting a threshold intensity and then applying a sigmoid function to it. Assuming identified regions consist of more than one pixel, CHIPS fits a Beta distribution over the probability space of the enclosed region and estimates its parameters. Finally, CHIPS extracts the final probability measure ( $\theta$ ) by integrating the area under the curve enclosed by the Beta distribution and a user-defined threshold and attaching it to the associated region of interest. The GitHub code base is available at <https://github.com/shibajit7/CHIPS>.

### Appendix C

#### WWWBCS: Warwick Wavelet Watershed-based Coronal Segmentation

The tool Warwick wavelet watershed-based coronal segmentation (WWWBCS), developed by E. Verwichte and C. Foullon, works as follows. For the coronal segmentation, the three AIA bandpasses that capture the bulk of the coronal plasma are used, i.e., 171 Å, 193 Å, and 211 Å. We focus on the solar disk. The three Level 1 AIA images are preprocessed so that they are normalized with respect to exposure time and pointing is matched with the 193 Å bandpass. The images are rescaled to  $512 \times 512$  resolution. The images have not been deconvolved using the AIA point-spread function, though that may be included in future iterations. To correct for LOS effects that are pronounced near the solar limb, a radial profile is used that is a fit to the azimuthal average intensity.

As large-scale features such as coronal holes have the greatest contrast in the 193 Å bandpass, this channel is used as

the reference. We build on the prominence detection scheme developed by Foullon & Verwichte (2006) that takes advantage of the temperature sensitivity of bandpass ratios to construct three parameters:






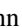









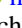




$$x = \frac{I_{171}}{I_{193}}, \quad y = \frac{I_{211}}{I_{193}}, \quad z = \ln(I_{193}). \quad (C1)$$

The parameters  $x$  and  $y$  reflect the cool and hot components of coronal plasma, and  $z$  is a measure of overall density (emission measure). However, the ratios are noisy when considered on a pixel-per-pixel level. Therefore, to increase the statistical significance the 193 Å image is first filtered and then segmented into coherent regions. For the filtering we use a continuous Mexican-hat wavelet transform (Witkin 1983). The Mexican-hat wavelet is the negative Laplacian of a Gaussian shape and enhances intensity pulses and ridges in images. In scale space, the transform will have a maximum response at the scale of the feature studied. It is therefore well suited to enhance the location of solar features including coronal loops (White & Verwichte 2012). Here, the wavelet transform is performed at a chosen fixed scale of around  $10''$ . The segmentation is realized using a seeded watershed transform on the gradient of the filtered image (Neubert & Protzel 2014). The resulting catchment basins (regions) tend to be internally uniform and separated from its neighbors by natural gradients in the image. For each region, the average intensity from the three bandpasses is used to construct the parameters  $x$ ,  $y$ , and  $z$ . The segmentation method has the added computational advantage of reducing the length of the parameter arrays from about 120,000, if it were pixel based on a  $512 \times 512$  image, to typically around 5000.

This process is repeated for over 300 sets of three contemporary AIA images, each separated by 13 days, from 2010 June. For every consecutive seven sets, the region parameters are combined so as to have a good representation of the major typical features on the solar disk: coronal holes, quiet-Sun and active regions. For each parameter the average and standard deviation is found in order to create standardized versions of the parameters,  $x_n$ ,  $y_n$ , and  $z_n$ . In this three-dimensional parameter space the regions are divided into three clusters using the  $k$ -means algorithm, which minimizes the Euclidean distance between the region parameters and centroids. The initial guess of the centroids are calculated by forward-modeling the DEM curve for coronal holes, quiet-Sun and active regions (Vernazza & Reeves 1978) to the intensity in the three AIA bandpasses and the subsequent parameters. Over the solar cycle, the values of averages, standard deviations, and centroid positions vary. A smooth curve is produced as a function of time for all these quantities using a Savitzky-Golay filter. These curves form a database that can be used to classify the solar disk at any time. For any set of three AIA images the unstandardized region parameter values are found using the segmentation method set out above. The interpolated values from the database curves are used to standardize and classify each region. A binary map of coronal holes is created by filling in all pixels in the regions classified as coronal hole.

#### ORCID iDs

Martin A. Reiss  <https://orcid.org/0000-0002-6362-5054>  
Karin Muglach  <https://orcid.org/0000-0002-5547-9683>

Emily Mason  <https://orcid.org/0000-0002-8767-7182>  
 Emma E. Davies  <https://orcid.org/0000-0001-9992-8471>  
 Shibaji Chakraborty  <https://orcid.org/0000-0001-6792-0037>  
 Cooper Downs  <https://orcid.org/0000-0003-1759-4354>  
 Tadhg M. Garton  <https://orcid.org/0000-0002-3031-2991>  
 Jeremy A. Grajeda  <https://orcid.org/0009-0008-3189-8200>  
 Stephan G. Heinemann  <https://orcid.org/0000-0002-2655-2108>  
 Stefan Hofmeister  <https://orcid.org/0000-0001-7662-1960>  
 Egor Illarionov  <https://orcid.org/0000-0002-2858-9625>  
 Robert Jarolim  <https://orcid.org/0000-0002-9309-2981>  
 Larisza Krista  <https://orcid.org/0000-0003-4627-8967>  
 Erwin Verwichte  <https://orcid.org/0000-0002-1723-1468>  
 Charles N. Arge  <https://orcid.org/0000-0001-9326-3448>  
 Laura E. Boucheron  <https://orcid.org/0000-0002-8187-1566>  
 Claire Foullon  <https://orcid.org/0000-0002-2532-9684>  
 Michael S. Kirk  <https://orcid.org/0000-0001-9874-1429>  
 Alexander Kosovichev  <https://orcid.org/0000-0003-0364-4883>  
 Andrew Leisner  <https://orcid.org/0000-0002-4752-7534>  
 Christian Möstl  <https://orcid.org/0000-0001-6868-4152>  
 James Turtle  <https://orcid.org/0000-0003-0735-7769>  
 Astrid Veronig  <https://orcid.org/0000-0003-2073-002X>

## References

- Arge, C. N., Leisner, A., Wallace, S., & Henney, C. J. 2023, arXiv:2304.07649  
 Arge, C. N., Odstrcil, D., Pizzo, V. J., & Mayer, L. R. 2003, in AIP Conf. Proc. 679, Solar Wind Ten, ed. M. Velli et al. (Melville, NY: AIP), 190  
 Arge, C. N., & Pizzo, V. J. 2000, *JGR*, 105, 10465  
 Badman, S. T., Bale, S. D., Rouillard, A. P., et al. 2021, *A&A*, 650, A18  
 Boucheron, L. E., Valluri, M., & McAteer, R. T. J. 2016, *SoPh*, 291, 2353  
 Caplan, R. M., Downs, C., & Linker, J. A. 2016, *ApJ*, 823, 53  
 Cranmer, S. R. 2009, *LRSPP*, 6, 3  
 de Toma, G. 2011, *SoPh*, 274, 195  
 de Wijn, A. G., Burkepile, J. T., Tomczyk, S., et al. 2012, *Proc. SPIE*, 8444, 844 43N  
 Delouille, V., Hofmeister, S. J., Reiss, M. A., et al. 2018, in Machine Learning Techniques for Space Weather, ed. E. Camporeale, S. Wing, & J. R. Johnson (New York: Elsevier), 365  
 Foullon, C., & Verwichte, E. 2006, *SoPh*, 234, 135  
 Frost, A. M., Owens, M., Macneil, A., & Lockwood, M. 2022, *SoPh*, 297, 82  
 Garton, T. M., Gallagher, P. T., & Murray, S. A. 2018, *JSWSC*, 8, A02  
 Grajeda, J. A., Boucheron, L. E., Kirk, M. S., Leisner, A., & Arge, C. N. 2023, *SoPh*, 298, 133  
 Hamada, A., Asikainen, T., Virtanen, I., & Mursula, K. 2018, *SoPh*, 293, 71  
 Harvey, K. L., & Recely, F. 2002, *SoPh*, 211, 31  
 Heinemann, S. G., Jerčić, V., Temmer, M., et al. 2020, *A&A*, 638, A68  
 Heinemann, S. G., Temmer, M., Heinemann, N., et al. 2019, *SoPh*, 294, 144  
 Heinemann, S. G., Temmer, M., Hofmeister, S. J., Veronig, A. M., & Vennerstrøm, S. 2018, *ApJ*, 861, 151  
 Henney, C. J., & Harvey, J. W. 2005, in ASP Conf. Ser. 346, Large-scale Structures and their Role in Solar Activity, ed. K. Sankarasubramanian, M. Penn, & A. Pevtsov (San Francisco, CA: ASP), 261  
 Hofmeister, S. J., Veronig, A., Reiss, M. A., et al. 2017, *ApJ*, 835, 268  
 Huber, M. C. E., Foukal, P. V., Noyes, R. W., et al. 1974, *ApJL*, 194, L115  
 Illarionov, E. A., & Tlatov, A. G. 2018, *MNRAS*, 481, 5014  
 Jarolim, R., Veronig, A. M., Hofmeister, S., et al. 2021, *A&A*, 652, A13  
 Kaiser, M. L. 2005, *AdSpR*, 36, 1483  
 Ko, Y.-K., Muglach, K., Wang, Y.-M., Young, P. R., & Lepri, S. T. 2014, *ApJ*, 787, 121  
 Krista, L. D., & Gallagher, P. T. 2009, *SoPh*, 256, 87  
 Krista, L. D., McIntosh, S. W., & Leamon, R. J. 2018, *AJ*, 155, 153  
 Lemen, J. R., Jr., Title, A. M., Akin, D. J., et al. 2012, *SoPh*, 275, 17  
 Linker, J. A., Caplan, R. M., Downs, C., et al. 2017, *ApJ*, 848, 70  
 Linker, J. A., Heinemann, S. G., Temmer, M., et al. 2021, *ApJ*, 918, 21  
 Lowder, C., Qiu, J., Leamon, R., & Liu, Y. 2014, *ApJ*, 783, 142  
 Lowder, C., Qiu, J., & Leamon, R. 2017, *SoPh*, 292, 18  
 Mackay, D. H., Priest, E. R., & Lockwood, M. 2002, *SoPh*, 209, 287  
 Mackay, D. H., & Yeates, A. R. 2012, *LRSPP*, 9, 6  
 Malanushenko, O. V., & Jones, H. P. 2005, *SoPh*, 226, 3  
 Mason, E. I., & Uritsky, V. M. 2022, *ApJL*, 937, L19  
 McComas, D. J., Velli, M., Lewis, W. S., et al. 2007, *RvGeo*, 45, RG1004  
 McIntosh, P. S. 2003, in ESA Special Publication 535, Solar Variability as an Input to the Earth's Environment, ed. A. Wilson (Noordwijk: ESA Publications Division), 807  
 Mikić, Z., Linker, J. A., Schnack, D. D., Lionello, R., & Tarditi, A. 1999, *PhPl*, 6, 2217  
 Munro, R. H., & Withbroe, G. L. 1972, *ApJ*, 176, 511  
 Nash, A. G., Sheeley, N. R., & Wang, Y. M. J. 1988, *SoPh*, 117, 359  
 Neubert, P., & Protzel, P. 2014, in Proc. of the 2014 22nd Int. Conf. on Pattern Recognition (Los Alamitos, CA: IEEE Computer Society), 996  
 Newkirk, G., Jr+ 1967, *ARA&A*, 5, 213  
 Nolte, J. T., Krieger, A. S., Timothy, A. F., et al. 1976, *SoPh*, 46, 303  
 Pesnell, W. D., Thompson, B. J., & Chamberlin, P. C. 2012, *SoPh*, 275, 3  
 Priest, E. 2014, Magnetohydrodynamics of the Sun (2nd ed.; New York: Cambridge Univ. Press)  
 Reiss, M., Arge, C. N., Henney, C. J., et al. 2023, *AdSpR*, in press  
 Reiss, M. A., Hofmeister, S. J., De Visscher, R., et al. 2015, *JSWSC*, 5, A23  
 Reiss, M. A., Muglach, K., Möstl, C., et al. 2021, *ApJ*, 913, 28  
 Reiss, M. A., Temmer, M., Veronig, A. M., et al. 2016, *SpWea*, 14, 495  
 Riley, P. 2007, *ApJL*, 667, L97  
 Riley, P., Linker, J. A., & Mikić, Z. 2001, *JGR*, 106, 15889  
 Riley, P., Linker, J. A., Mikić, Z., et al. 2019, *ApJ*, 884, 18  
 Robbins, S., Henney, C. J., & Harvey, J. W. 2006, *SoPh*, 233, 265  
 Rotter, T., Veronig, A. M., Temmer, M., & Vršnak, B. 2012, *SoPh*, 281, 793  
 Saqri, J., Veronig, A. M., Heinemann, S. G., et al. 2020, *SoPh*, 295, 6  
 Scherrer, P. H., Schou, J., Bush, R. I., et al. 2012, *SoPh*, 275, 207  
 Scholl, I. F., & Habbal, S. R. 2008, *SoPh*, 248, 425  
 Timothy, A. F., Krieger, A. S., & Vaiana, G. S. 1975, *SoPh*, 42, 135  
 Toma, G. D., & Arge, C. N. 2005, in ASP Conf. Ser. 346, Large-scale Structures and their Role in Solar Activity, ed. K. Sankarasubramanian, M. Penn, & A. Pevtsov (San Francisco, CA: ASP), 251  
 Tóth, G., Sokolov, I. V., Gombosi, T. I., et al. 2005, *JGRA*, 110, A12226  
 Tousey, R., Sandlin, G. D., & Purcell, J. D. 1968, in IAU Symp. 35, Structure and Development of Solar Active Regions, ed. K. O. Kiepenheuer (Dordrecht: D. Reidel), 411  
 van der Holst, B., Sokolov, I. V., Meng, X., et al. 2014, *ApJ*, 782, 81  
 Verbeeck, C., Delouille, V., Mampaey, B., & De Visscher, R. 2014, *A&A*, 561, A29  
 Vernazza, J. E., & Reeves, E. M. 1978, *ApJS*, 37, 485  
 Viall, N. M., & Borovsky, J. E. 2020, *JGRA*, 125, e26005  
 Vršnak, B., Temmer, M., & Veronig, A. M. 2007, *SoPh*, 240, 315  
 Wallace, S., Arge, C. N., Pattichis, M., Hock-Mysliwiec, R. A., & Henney, C. J. 2019, *SoPh*, 294, 19  
 Wang, Y. M. 2009, *SSRv*, 144, 383  
 Wang, Y. M. 2017, *ApJ*, 841, 94  
 Wang, Y. M., Robbrecht, E., & Muglach, K. 2011, *ApJ*, 733, 20  
 Wang, Y. M., Robbrecht, E., Rouillard, A. P., Sheeley, N. R., & Thernisien, A. F. R. J. 2010, *ApJ*, 715, 39  
 Wang, Y.-M., & Sheeley, N. R., Jr+ 1990, *ApJ*, 355, 726  
 Wang, Y.-M., & Sheeley, N. R., Jr+ 1993, *ApJ*, 414, 916  
 Wang, Y. M., & Sheeley, N. R., Jr. 2015, *ApJL*, 809, L24  
 Wang, Y. M., Sheeley, N. R., Jr., & Howard, R. A. 1997, *ApJ*, 485, 875  
 Wang, Y. M., Ulrich, R. K., & Harvey, J. W. 2022, *ApJ*, 926, 113  
 White, R. S., & Verwichte, E. 2012, *A&A*, 537, A49  
 Witkin, A. 1983, Proc. 8th Int. Joint Conf. Artificial Intelligence, Vol. 2, ed. A. Bundy (International Joint Conference on Artificial Intelligence), 1019, <https://www.ijcai.org/Proceedings/83-2/Papers/091.pdf>  
 Woods, T. N., Eparvier, F. G., Hock, R., et al. 2012, *SoPh*, 275, 115  
 Yeates, A. R., Mackay, D. H., van Ballegooijen, A. A., & Constable, J. A. 2010, *JGRA*, 115, A09112  
 Zirker, J. B. 1977, *RvGSP*, 15, 257